SOLAR RADIATION PRESSURE, DRAG AND GRAVITATIONAL EFFECTS ON A DUST PARTICLE IN EARTH ORBIT

BY

BINDU BHARGAVI JAGANNATHA

THESIS

Submitted in partial fulfillment of the requirements
for the degree of Master of Science in Aerospace Engineering
in the Graduate College of the
University of Illinois at Urbana-Champaign, 2012

Urbana, Illinois

Adviser:

Professor Victoria L. Coverstone

Abstract

This work aims to further the research done on evaluating the effects of various perturbing forces on Earth-orbiting particles by numerical integration. One of the predominant perturbations on particle orbits is the solar radiation pressure (SRP), which is defined as the pressure exerted by the photons constituting the light from the Sun. Colombo et. al [1] studied the orbital dynamics of "smart-dust" under the effects of SRP and atmospheric drag. The numerical model developed here will expand on that work, but will use Hamiltonian equations of motion instead of Gauss equations. This approach easily incorporates forces such as drag, SRP and J_2 perturbations. Solar radiation pressure is switched off while the particle passes through the Earth's shadow. The model is developed in an Earth-Centric Inertial frame, where the Sun and the Moon are averaged to lie in the ecliptic plane with an obliquity of 23.6°. None of the effects of perturbation are averaged, thus this study can provide the entire set of initial orbital elements of particles in Earth-orbit required to ensure a long lifespan. The differential equations of motion are numerically integrated using MATLAB's pre-packaged `ode45`. These formulations and assumptions are tested against results found in existing literature.

The application of this model so far described is to select a set of initial orbital elements that will balance the dissipative effects of drag with coupling of SRP, J_2 and Moon's gravity, thereby ensuring longer orbital lifetimes. The methodology employs Montecarlo simulations over the possible regime of some known initial conditions, while varying the others. A "goldilocks" region is chosen by superimposing the results from different Montecarlo runs that produce the least departure from the initial set of orbital elements at the end of one simulated orbit. These orbits are conjectured to have the longest lifespans; in a sample calculation, the orbital lifetime was increased by 30 times by selecting a set of initial elements from this "goldilocks" region, as compared to an arbitrary set of initial conditions outside it.

The eventual goal of this work is to aid precise orbital propagation of swarms of nano-satellites through the use of heavier computational resources. Due to the non-specific nature of all parameters used, this model can also be utilized for missions at other planetary bodies or those in lunar orbit. Inclusion of higher-order integrators or variational integrators (over the Runge-Kutta methods used here) may improve accuracy.

Acknowledgements

I would not be able to graduate without the support of many people. Heartfelt thanks to my advisor, Victoria Coverstone, for her unlimited patience and for all the opportunities she has provided to me. Without her belief in me and her words of kindness and encouragement, this thesis would be lost. Her scientific insight and questions have taught me something new every time I talk to her. Also thanks to all my teachers at the University of Illinois who have rekindled my delight in learning.

I am also fortunate to have friends who believed more in me than I did sometimes – Bhargav, Vicky and Donald.

My parents and my sister have always been my guiding light; I'm extremely grateful to them for molding me into what I am today and for all the sacrifices they have made for me. And of course, to Hari, who puts all things in perspective by laughing while I cry. The world seems a little less daunting with him on my side.

Table of Contents

List of Figures

List of Tables

List of Abbreviations, Symbols and Constants

List of Abbreviations

CCM	Cartesian Coordinate Module
COE	Classical Orbital Elements
CW	Clock wise
CCW	Counterclock wise
ECI	Earth-Centered Inertial
EOM	Equations of Motion
RHS	Right Hand Side
SRP	Solar Radiation Pressure
SCM	Spherical Coordinate Module

List of Symbols

m	Mass of satellite orbiting Earth
A	Area of satellite orbiting Earth
$\mu_{\oplus}$	Gravitational constant of Earth
$\mu_{\leftmoon}$	Gravitational constant of Moon
$a_{\leftmoon}$	Semi-major axis of Moon's orbit around Earth
λ	Angle of the Sun-line with reference axis
γ	Angle of the Moon-line with reference axis
ϵ	Obliquity of the ecliptic
ρ_{air}	Atmospheric density

List of Subscripts

$\oplus$	Earth
$\odot$	Sun
$\leftmoon$	Moon
x	Component in $\hat{i}$-direction
y	Component in $\hat{j}$-direction
z	Component in $\hat{k}$-direction
r	Component in $\hat{r}$-direction
θ	Component in $\hat{\theta}$-direction
ϕ	Component in $\hat{\phi}$-direction

List of Superscripts

$\vec{}$	Vector
$\hat{}$	Unit vector

List of Constants

$\mu_\oplus$	$= 3.986\times10^5$ km^3/s^2
$\mu_{\leftmoon}$	$= 4.903\times10^3$ km^3/s^2
$a_{\leftmoon}$	$= 3.844\times10^5$ km
$R_\oplus$	$= 6378.16$ km
J_2	$= 1082.63 \times 10^{-6}$
ϵ	$= 23.4\ ^\circ$

Chapter 1

INTRODUCTION

In an idealized two-body problem formulation, the orbital elements are easily determined since the body in orbit is acted upon only by the gravitational forces of the central body. However, in reality, every satellite is subjected to various perturbations like drag, oblateness of the central body, third-body gravitational effects, radiation pressure, electromagnetic forces, thrust, etc. and thus deviate from their ideal Keplerian orbit. Oblateness effects arise due to nonuniform distribution of mass as a result of the central body not being perfectly spherical. Gravitational potential from this nonuniform mass distribution is commonly represented using the Legendre polynomial expansion and J_2 is the coefficient of the first term in this expansion. Electromagnetic attractions/repulsions are caused by residual charge/magnetism on interacting bodies. This kind of interaction has been recorded in interplanetary plasmas and among the particles that constitute the planetary rings; however, this force will not be considered in the present study. In the case of a body in Earth orbit, some of the dominant perturbations are atmospheric drag, J_2, solar radiation pressure and third-body gravitational attraction from the Moon – the effects of these forces are being examined in this thesis.

Solar radiation pressure arises from the particulate nature of light – it is the pressure experienced by any material object placed in the path of solar-photon flow [4]. In the outer reaches of the atmosphere, as the effects of drag diminish, the perturbations due to solar radiation pressure (SRP) become more prominent. In 1960, the unexplained perturbations of 1-2 km in perigee height (with a period of 850 days) of Vanguard I were attributed to the effect of solar radiation pressure [5]. The same reference calculates the effective area-to-mass ratio of Vanguard I to be 0.0212 m^2/kg. Micrometer-sized particles are even more susceptible to the perturbations by SRP and the formation of the rings of Saturn and other giant planets are theorised to be heavily influenced by it [6]. Depending on the direction of the velocity and the radius vector of the body in orbit, SRP can display dissipative as well as additive behaviour. Larger satellites are equipped with station-keeping thrusters and any decay in orbit can be adjusted to achieve the desired lifespan.

In the recent past, the interest in satellite constellation design has been on a rise due to advantage gained by larger spatial coverage and disposability [7]. Evolving techniques from the electronic industry,

and by extension from MEMS technologies, allow miniaturization of each member of the swarm to achieve considerable benefits in terms of cost-to-manufacture and cost-to-launch [8]. This however compromises on individual propulsive capabilities, thereby lowering lifespan. Solar-sail demonstrations such as IKAROS have proven SRP as a feasible propulsive technology. Using a similar idea, Colombo et. al. [1, 9] have tried to exploit solar radiation pressure to counter the drag effects on 'SpaceChips', enabling longer orbital lifetimes without active control. This thesis extends that analysis to include more perturbing forces, while reducing simplifying assumptions and simulating the entire lifetime without averaging over mean motion. The ultimate motive is to pick and select initial conditions that increase scientific return by leading to longer lifespans; in the present analysis, this is achieved via Montecarlo simulations.

The satellites considered in this work have an area-to-mass ratio in the range of $17 - 55$ m^2/kg. At such high ratios, the drag and solar radiation pressure are the most dominant forces; it is their coupling with the oblateness and third-body effects that is being exploited here to increase lifespans. The third-body effects are minimal, but have been included because this work was initially geared at explaining the formation of planetary rings, where small moons interleave between the rings and shepherd the ring particles. The model is set-up and the derivations of the Hamiltonian equations and its components in Earth-Centered Inertial (ECI) frame are shown in Chapter 2. For ease of adding a greater variety of perturbing forces, spherical coordinates have been given preference in this work over classical orbital elements and equinoctial elements.

This model is validated against existing studies in Chapter 4. The equations of motion can be derived in either the Cartesian or spherical coordinates. The spherical coordinate system is amenable to use the spherical harmonic treatment of Earth's gravitational field (required to include J_2 perturbations); however, using angles instead of distances implicitly gives rise to singularities if sine or cosine is used in the denominator. Cartesian coordinates are easier to manipulate and suffer no singularities. The choice of spherical coordinate system as the principal mode is justified in Section 4.1.

The manner of application of this method and the results are presented in Chapter 5. As mentioned earlier, the method of selecting those initial conditions which ensure longevity of resulting orbits is by using the Montecarlo method. In this thesis, the perigee height and inclination are chosen to be 669.4152 km and 51.6°. The perigee height corresponds to the value used in Colombo [1] and hence makes for easier comparison. The particular value of inclination is equal to that of the ISS orbit. It can be envisioned that future swarms of satellites would be released from the space station. Phase-space diagrams are plotted for changes in orbital elements at the end of the first orbit. And finally, from these plots, the required initial classical orbital elements are found.

Chapter 2

SYSTEM MODEL

The system under consideration is a particle in orbit around Earth, whose orbital trajectory needs to be calculated while under the influence of four perturbing forces - atmospheric drag, SRP, Earth's J_2 and Moon's gravitational attraction. SRP and drag are proportional to the area-by-mass ratio, while the oblateness and third-body effects vary with just the mass of the orbiting body. This set-up is treated as a two-body problem in this study, where the Earth is the (central) primary body and the satellite is the secondary body. The origin for the coordinate system is at the center of the Earth, while the X-axis is fixed as pointing to the First Point in Aries in order to make the ecliptic calculations easier, Z-axis passes through the Earth's north pole and Y-axis is found from the right-hand rule.

The other choice in frame of reference would be the one with its origin at the center of mass of the Earth-Moon system, since third-body perturbations can then be expressed as a potential in Hamiltonian of the system; however, this would impede the easy calculations of the other perturbations. The ECI frame lends itself better to the calculations of drag, solar radiation and J_2 forces felt by the satellite.

If Earth's orbit around the Sun and the Moon's orbit around the Earth are assumed circular, then both the Sun and the Moon can be equivalently interpreted to go around the Earth at constant rates - the Sun in a clockwise direction, while the Moon in an anti-clockwise orbit. Ignoring the nominal 5° inclination of the Moon's orbit to the ecliptic, the Sun and the Moon are represented to be in the same plane. In this work, the obliquity of the ecliptic is set at 23.6°. An exponential model of the atmospheric density is used, while also assuming that the atmosphere rotates with the Earth. The effect of Earth's shadow is included in the SRP calculations – the magnitude of this force is constant while in light, and equal to zero while in shadow.

The limitation of this analysis originates in treating this system as a two-body problem, with external gravitational perturbations, rather than a three-body problem (discussed in further detail in Section 2.5). The described model is valid only until the point where acceleration due to central body's gravity is greater than the magnitude of perturbation from the third-body.

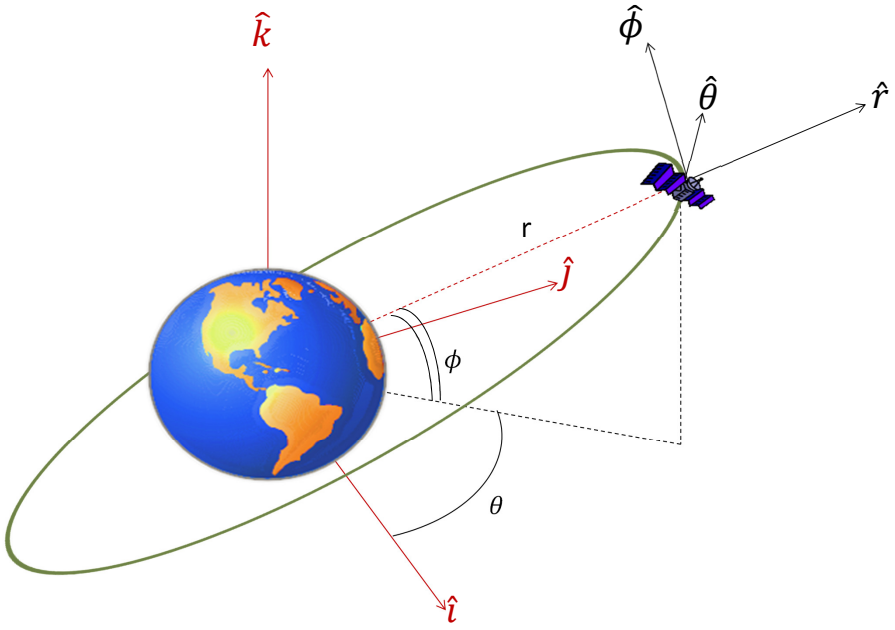

Figure 2.1: Relation between Spherical ($\hat{r} - \hat{\theta} - \hat{\phi}$) and Cartesian ($\hat{\imath} - \hat{\jmath} - \hat{k}$) coordinate systems, showing an example satellite in Earth-orbit

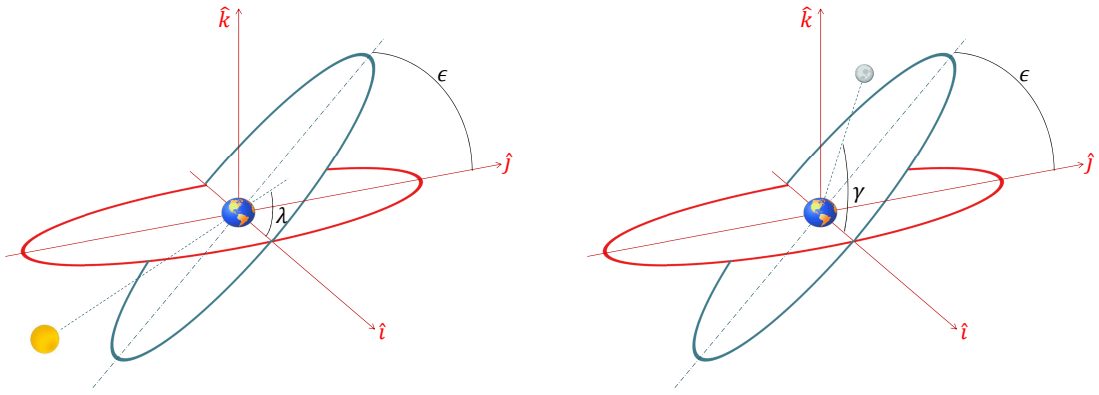

(a) (b)

Figure 2.2: Relative positions of the bodies involved in the model : (a) Earth and Sun (b) Earth and Moon

2.1 Equations of Motion

Newton's Second Law, which says change in momentum is equal to the total force applied, serves as the backbone for deriving the equations of motion (EOM). Hamiltonian equations of motion, an equivalent formulation of Newton's Second Law, can be used to provide $2n$ first-order ODEs describing the motion of this particle, where n = degree of freedom.

If the complete configuration of the system can be described by using n generalized coordinates q_i, then the Lagrangian function $\mathcal{L}(q, \dot{q}, t)$ can be defined as

$$\mathcal{L} = T - V$$

where T = kinetic energy and V = potential energy. The generalized momentum p_i corresponding to the generalized coordinate q_i is given by

$$p_i = \frac{\partial \mathcal{L}}{\partial \dot{q}_i}$$

The Hamiltonian function $\mathcal{H}(p, q, t)$ is another way of describing the energy of the system, but the Hamiltonian uses momenta to describe kinetic energy, instead of "generalized velocities". It is defined as:

$$\mathcal{H} = \sum p_i \dot{q}_i - \mathcal{L}$$

Finally, Hamilton's canonical equations of motion for any given holonomic system can be derived as^{Ref}:

$$\dot{q}_i = \frac{\partial \mathcal{H}}{\partial p_i}$$

$$\dot{p}_i = -\frac{\partial \mathcal{H}}{\partial q_i} + F_i$$

where F_i = generalized applied force which is not derivable from a potential function.

Using the above formulation, the Hamiltonian function for the present system can be derived by using r, ϕ, θ or x, y, z as generalized coordinates. The kinetic energy is a straightforward expression; however the potential energy due to Earth's gravity has to include oblateness terms.

EOM in Spherical Coordinates

If R = radius of the central body, the gravitational potential of this axially symmetric body is written as [10]:

$$U = \frac{\mu}{r}\left\{1 - \sum_{n=2}^{\infty} J_n \left(\frac{R}{r}\right) P_n(\sin\phi)\right\}$$

where ϕ = complement of colatitude (angle measured from the $\hat{i}-\hat{j}$ plane) and P_n = Legendre polynomials of nth order.

Since the present oblateness analysis accounts for only the J_2 term, the Earth's potential is expressed as the following to extract the potential energy of a particle in orbit:

$$P_2 = \frac{3\sin^2\phi - 1}{2} = \frac{2 - 3\cos^2\phi}{2}$$

$$\Rightarrow U_{\oplus} = \frac{\mu}{r}\left\{1 - J_2\left(\frac{R_{\oplus}}{r}\right)^2\left(1 - \frac{3\cos^2\phi}{2}\right)\right\}$$

From this, the potential energy can be worked out and in turn, the Hamiltonian of the system.

$$T = \frac{m}{2}\left[\dot{r}^2 + (r\dot{\phi})^2 + (r\cos\phi\ \dot{\theta})^2\right]$$
$$V = -\frac{\mu_{\oplus} m}{r} + \frac{\mu_{\oplus} m J_2}{r}\left(\frac{R_{\oplus}}{r}\right)^2\left[1 - \frac{3\cos^2\phi}{2}\right]$$
$$\mathcal{L} = \frac{m}{2}\left[\dot{r}^2 + (r\dot{\phi})^2 + (r\cos\phi\ \dot{\theta})^2\right] + \frac{\mu_{\oplus} m}{r} - \frac{\mu_{\oplus} m J_2}{r}\left(\frac{R_{\oplus}}{r}\right)^2\left[1 - \frac{3\cos^2\phi}{2}\right]$$

$$\Rightarrow \mathcal{H} = \frac{1}{2m}\left[p_r^2 + (\frac{p_\phi}{r})^2 + (\frac{p_\theta}{r\cos\phi})^2\right] - \frac{\mu_{\oplus} m}{r} + \frac{\mu_{\oplus} m J_2 R_{\oplus}^2}{r^3}\left[1 - \frac{3\cos^2\phi}{2}\right] \tag{2.1}$$

The generalized forces acting on this system are denoted as F_{SRP} (solar radiation pressure), D (atmospheric drag) and M (Moon's gravitational perturbations). Therefore, the Hamiltonian EOM of an Earth satellite in spherical coordinates are:

$$\dot{r} = \frac{p_r}{m} \tag{2.2a}$$

$$\dot{p_r} = \frac{p_\phi^2}{mr^3} + \frac{p_\theta^2}{mr^3\cos^2\phi} - \frac{\mu_{\oplus} m}{r^2} + \frac{3\mu_{\oplus} m J_2 R_{\oplus}^2}{r^4}\left[1 - \frac{3\cos^2\phi}{2}\right] + F_{SRP_r} + D_r + M_r \tag{2.2b}$$

$$\dot{\theta} = \frac{p_\theta}{mr^2\cos^2\phi} \tag{2.2c}$$

$$\dot{p_\theta} = (F_{SRP_\theta} + D_\theta + M_\theta)\cdot r\ \cos\phi \tag{2.2d}$$

$$\dot{\phi} = \frac{p_\phi}{mr^2} \tag{2.2e}$$

$$\dot{p_\phi} = -\frac{p_\theta^2 \sin\phi}{mr^2\cos^3\phi} - \frac{3\mu_\oplus m J_2 R_\oplus^2}{r^3}\sin\phi\cos\phi + (F_{SRP_\phi} + D_\phi + M_\phi)\cdot r \tag{2.2f}$$

EOM in Cartesian coordinates

As derived before,

$$U_\oplus = \frac{\mu_\oplus}{r}\left\{1 - J_2\left(\frac{R_\oplus}{r}\right)^2\left(\frac{2-3\cos^2\phi}{2}\right)\right\}$$

$$\Rightarrow U_\oplus = \frac{\mu_\oplus}{\sqrt{x^2+y^2+z^2}}\left\{1 - J_2\left(\frac{R_\oplus}{\sqrt{x^2+y^2+z^2}}\right)^2\left[1-\frac{3}{2}\left(\frac{x^2+y^2}{x^2+y^2+z^2}\right)\right]\right\}$$

From this, the potential energy can be written down and in turn, the Hamiltonian of the system.

$$T = \frac{m}{2}\left[\dot{x}^2+\dot{y}^2+\dot{z}^2\right]$$

$$V = -\frac{\mu_\oplus m}{\sqrt{x^2+y^2+z^2}} + \frac{\mu_\oplus m J_2}{\sqrt{x^2+y^2+z^2}}\left(\frac{R_\oplus}{\sqrt{x^2+y^2+z^2}}\right)^2\left[1-\frac{3}{2}\left(\frac{x^2+y^2}{x^2+y^2+z^2}\right)\right]$$

$$\mathcal{L} = \frac{m}{2}\left[\dot{x}^2+\dot{y}^2+\dot{z}^2\right] + \frac{\mu_\oplus m}{\sqrt{x^2+y^2+z^2}} - \frac{\mu_\oplus m J_2}{\sqrt{x^2+y^2+z^2}}\left(\frac{R_\oplus}{\sqrt{x^2+y^2+z^2}}\right)^2\left[1-\frac{3}{2}\left(\frac{x^2+y^2}{x^2+y^2+z^2}\right)\right]$$

$$\Rightarrow \mathcal{H} = \frac{1}{2m}\left[p_x^2+p_y^2+p_z^2\right] - \frac{\mu_\oplus m}{\sqrt{x^2+y^2+z^2}} + \frac{\mu_\oplus m J_2 R_\oplus^2}{(x^2+y^2+z^2)^{3/2}}\left[1-\frac{3}{2}\left(\frac{x^2+y^2}{x^2+y^2+z^2}\right)\right] \tag{2.3}$$

After some algebraic manipulation, the Hamiltonian EOM of any Earth satellite in Cartesian coordinates are:

$$\dot{x} = \frac{p_x}{m} \tag{2.4a}$$

$$\dot{p_x} = -\frac{\mu_\oplus m x}{(x^2+y^2+z^2)^{3/2}} + \frac{3\mu_\oplus m J_2 R_\oplus^2 x}{(x^2+y^2+z^2)^{5/2}}\left[1-\frac{1}{2}\left(\frac{3x^2+3y^2-2z^2}{x^2+y^2+z^2}\right)\right] + F_{SRP_x} + D_x + M_x \tag{2.4b}$$

$$\dot{y} = \frac{p_y}{m} \tag{2.4c}$$

$$\dot{p_y} = -\frac{\mu_\oplus m y}{(x^2+y^2+z^2)^{3/2}} + \frac{3\mu_\oplus m J_2 R_\oplus^2 y}{(x^2+y^2+z^2)^{5/2}}\left[1-\frac{1}{2}\left(\frac{3x^2+3y^2-2z^2}{x^2+y^2+z^2}\right)\right] + F_{SRP_y} + D_y + M_y \tag{2.4d}$$

$$\dot{z} = \frac{p_z}{m} \tag{2.4e}$$

$$\dot{p_z} = -\frac{\mu_\oplus m z}{(x^2+y^2+z^2)^{3/2}} + \frac{3\mu_\oplus m J_2 R_\oplus^2 z}{(x^2+y^2+z^2)^{5/2}}\left[1-\frac{7}{2}\left(\frac{x^2+y^2}{x^2+y^2+z^2}\right)\right] + F_{SRP_z} + D_z + M_z \tag{2.4f}$$

The components of these generalized forces in both coordinate systems are derived in the succeeding sections.

2.2 Direction of $\mathbf{F}_{SRP}$

This analysis assumes that the acceleration due to solar radiation pressure (SRP) is constant while the particle is in sunlight, and is equal to zero while it is in the Earth's shadow. Area exposed to the Sun is kept constant; in real life, this constraint translates to keeping the attitude of the orbiting body constant with respect to the Sun, or, in case of a small particle, that it has a spherical shape. At a distance of 1 AU, the force due to SRP is given by [4]:

$$F_{SRP} = p_{SR} c_R A$$

where p_{SR} (solar pressure) $= 4.56 \times 10^{-6}$ N/m^2, c_R = reflectivity coefficient and A = area exposed to the Sun (considered constant).

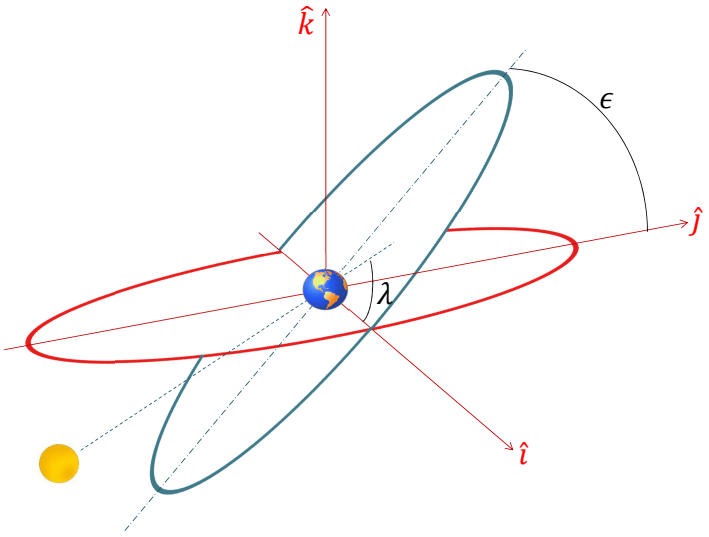

Figure 2.3: Position of the Sun on the ecliptic plane. The ecliptic plane is represented in blue and the Earth-equatorial frame $(\hat{\imath} - \hat{j})$ in red. λ = angle that the Sun-line makes with $\hat{\imath}$ and ϵ = obliquity of the ecliptic.

All perturbing forces must be expressed as the vector sum of their individual components in the respective coordinate system for use in Eq. 2.2 or 2.4. If λ denotes the angle the Sun-line makes with the X-axis of the (Cartesian) base frame as shown in Figure 2.3, then

$$\vec{F}_{SRP} = F_{SRP} \left\{ \cos\lambda \, \hat{\imath} + \cos\epsilon \sin\lambda \, \hat{j} + \sin\epsilon \sin\lambda \, \hat{k} \right\} \tag{2.5}$$

where $F_{SRP} = |\vec{F}_{SRP}| = p_{SR} C_R A$.

$$\therefore \vec{F}_{SRP_x} = F_{SRP} \cos\lambda \tag{2.6a}$$

$$\vec{F}_{SRP_y} = F_{SRP} \cos\epsilon \sin\lambda \tag{2.6b}$$

$$\vec{F}_{SRP_z} = F_{SRP} \sin\epsilon \sin\lambda \tag{2.6c}$$

Considering Figure 2.1, the $\hat{i} - \hat{j} - \hat{k}$ frame can be expressed in spherical coordinates $(\hat{r} - \hat{\theta} - \hat{\phi})$ as:

$$\begin{bmatrix} \hat{r} \\ \hat{\theta} \\ \hat{\phi} \end{bmatrix} = \begin{bmatrix} \cos\phi\ \cos\theta & \cos\phi\ \sin\theta & \sin\phi \\ -\sin\theta & \cos\theta & 0 \\ -\sin\phi\ \cos\theta & -\sin\phi\ \sin\theta & \cos\phi \end{bmatrix} \begin{bmatrix} \hat{i} \\ \hat{j} \\ \hat{k} \end{bmatrix} \tag{2.7}$$

$$\Rightarrow \begin{bmatrix} \hat{i} \\ \hat{j} \\ \hat{k} \end{bmatrix} = \begin{bmatrix} \cos\phi\ \cos\theta & -\sin\theta & -\sin\phi\ \cos\theta \\ \cos\phi\ \sin\theta & \cos\theta & -\sin\phi\ \sin\theta \\ \sin\phi & 0 & \cos\phi \end{bmatrix} \begin{bmatrix} \hat{r} \\ \hat{\theta} \\ \hat{\phi} \end{bmatrix} \tag{2.8}$$

This equation can be used to substitute for $\hat{i},\ \hat{j}$ and $\hat{k}$ in Eq. 2.5:

$$\begin{aligned} \vec{F}_{SRP} = {} & F_{SRP}\ (\cos\phi\cos\theta\cos\lambda\ +\ \cos\phi\sin\theta\sin\lambda\cos\epsilon + \sin\phi\sin\lambda\sin\epsilon)\ \hat{r}\ + \\ & F_{SRP}\ (-\ \sin\theta\cos\lambda\ +\ \cos\theta\sin\lambda\cos\epsilon\ )\ \hat{\theta}\ + \\ & F_{SRP}\ (-\sin\phi\cos\theta\cos\lambda\ -\ \sin\phi\sin\theta\sin\lambda\cos\epsilon\ +\ \cos\phi\sin\lambda\sin\epsilon)\ \hat{\phi} \end{aligned}$$

Therefore, the three components of F_{SRP} in spherical coordinates are:

$$F_{SRP_r} = F_{SRP}\ (\sin\phi\cos\theta\cos\lambda\ +\ \sin\phi\sin\theta\sin\lambda\cos\epsilon\ +\ \cos\phi\sin\lambda\sin\epsilon) \tag{2.9a}$$

$$F_{SRP_\theta} = F_{SRP}\ (\sin\lambda\cos\theta\cos\epsilon\ -\ \cos\lambda\sin\theta) \tag{2.9b}$$

$$F_{SRP_\phi} = F_{SRP}\ (-\cos\phi\cos\theta\cos\lambda\ -\ \cos\phi\sin\theta\sin\lambda\cos\epsilon\ +\ \sin\phi\sin\lambda\sin\epsilon) \tag{2.9c}$$

It must be noted that λ changes as the Earth goes around the Sun, hence it's value is changed according to $\lambda = \lambda_i - n_\odot t$, where λ_i = initial angle of the Sun-line and $n_\odot$ = constant rate (in rad/sec) at which the Earth goes around the Sun. This is in accordance with the assumption that the Earth's orbit is circular. It accounts for the apparent motion of the Sun around the Earth in a counter-clockwise direction (since Earth goes round the Sun in a clockwise manner).

2.3 Shadow Check

Figure 2.4(a) clearly illustrates that any particle in Earth-orbit will periodically enter the Earth's shadow, at which point it will not be subjected to solar radiation pressure until it exits the shadow region. It is reasonable to assume that the Sun is at an infinite distance and hence ignore the parallax of the Sun [1]. At the considered orbits, it is reasonable to expect a cylindrical shadow behind the Earth, with no penumbra, and of radius equal to the Earth's radius.

If $x',\ y',\ z'$ are the components of the position of the particle in the $\hat{i}' - \hat{j}' - \hat{k}'$ frame, the following conditions fall out of this setup, that enable the verification of the presence of the satellite in the Earth's shadow:

1. $x' > 0$
2. $\sqrt{y'^2 + z'^2} < R_{\oplus}$

The first condition checks that the particle is on the opposite side of Earth as the Sun, while the second one ensures its position lies within the cylindrical envelope presumed to be the Earth's shadow.

Now consider the frames $\hat{i} - \hat{j} - \hat{k}$ (equatorial) and $\hat{i}' - \hat{j}' - \hat{k}'$ (ecliptic) as shown in Figure 2.4(b). The rotation matrix between these frames, can be found as:

$$\begin{bmatrix} \hat{i}' \\ \hat{j}' \\ \hat{k}' \end{bmatrix} = \begin{bmatrix} \cos\lambda & \cos\epsilon\sin\lambda & \sin\epsilon\sin\lambda \\ -\sin\lambda & \cos\epsilon\cos\lambda & \sin\epsilon\cos\lambda \\ 0 & -\sin\epsilon & \cos\epsilon \end{bmatrix} \begin{bmatrix} \hat{i} \\ \hat{j} \\ \hat{k} \end{bmatrix} \tag{2.10}$$

$$\begin{aligned} \therefore x' &= x\cos\lambda + y\cos\epsilon\sin\lambda \ + z\sin\epsilon\sin\lambda \\ y' &= -x\sin\lambda + y\cos\epsilon\cos\lambda + z\sin\epsilon\cos\lambda \\ z' &= -y\sin\epsilon + z\cos\epsilon \end{aligned}$$

Cartesian coordinates of the particle's position in ECI reference frame can be written in terms of the spherical coordinates as follows:

$$\begin{aligned} x &= r\cos\phi\cos\theta \\ y &= r\cos\phi\sin\theta \\ z &= r\sin\phi \end{aligned}$$

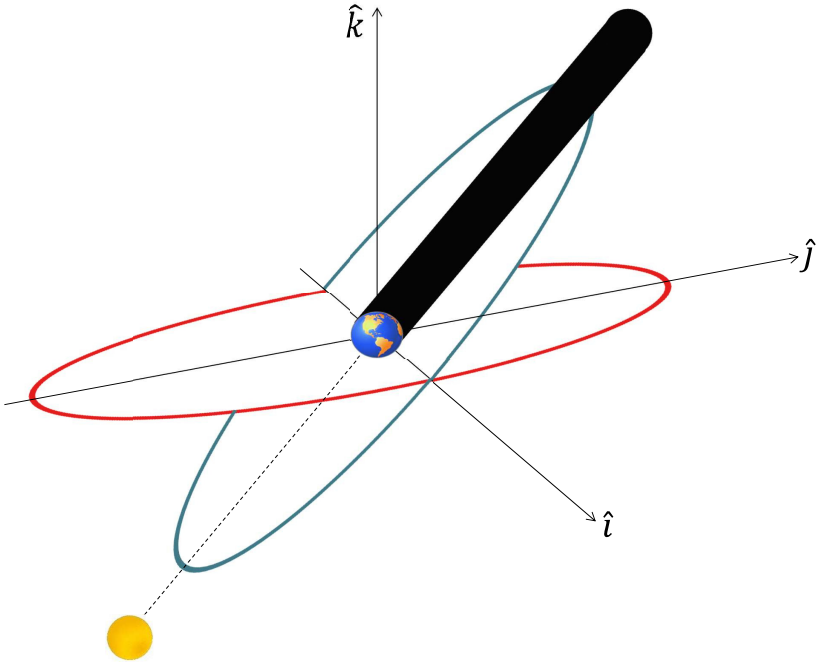

(a)

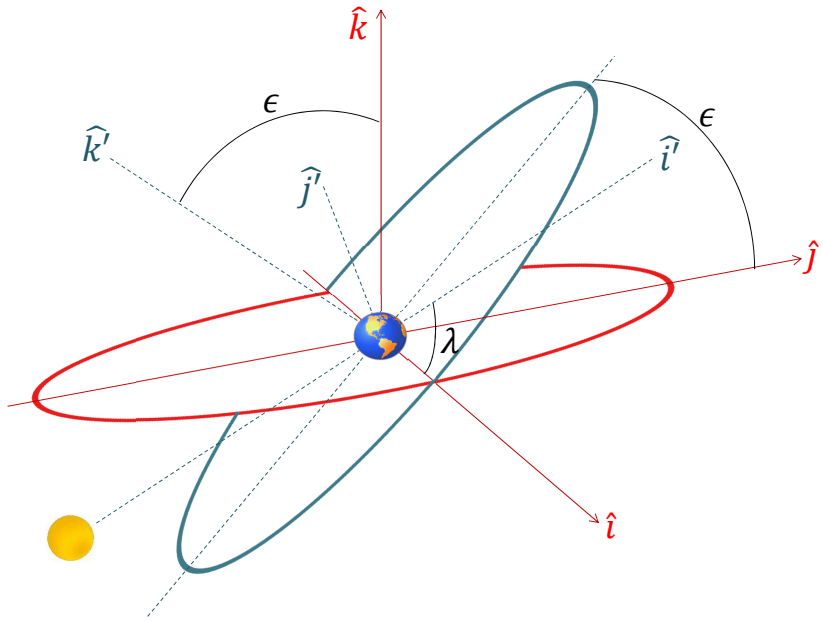

(b)

Figure 2.4: Illustration of the Earth's shadow under assumed conditions (red = Earth's equatorial plane, blue = ecliptic plane) (a) Position of the shadow (b) Frames involved in calculation of shadow conditions

$$\therefore x' = r[\cos\lambda\cos\phi\cos\theta + \cos\epsilon\sin\lambda\cos\phi\sin\theta \ + \sin\epsilon\sin\lambda\sin\phi]$$

$$y' = r[-\sin\lambda\cos\phi\cos\theta + \cos\epsilon\cos\lambda\cos\phi\sin\theta + \sin\epsilon\cos\lambda\sin\phi]$$

$$z' = r[-\sin\epsilon\cos\phi\sin\theta + \cos\epsilon\sin\phi]$$

In spherical coordinates, the conditions for shadow then translate to:

1. $(\cos\lambda\cos\phi\cos\theta + \cos\epsilon\sin\lambda\cos\phi\sin\theta \ + \sin\epsilon\sin\lambda\sin\phi) > 0$
2. $\sqrt{\{-\sin\lambda\cos\phi\cos\theta + \cos\epsilon\cos\lambda\cos\phi\sin\theta + \sin\epsilon\cos\lambda\sin\phi\}^2 + \{-\sin\epsilon\cos\phi\sin\theta + \cos\epsilon\sin\phi\}^2} < R_\oplus/r$

Or correspondingly in Cartesian coordinates:

1. $x\cos\lambda + y\sin\lambda\cos\epsilon + z\sin\lambda\sin\epsilon > 0$
2. $\sqrt{(-x\sin\lambda + y\cos\lambda\cos\epsilon + z\cos\lambda\sin\epsilon)^2 + (-y\sin\epsilon + z\cos\epsilon)^2} < R_\oplus$

2.4 Direction of Drag

The magnitude of atmospheric drag acting on a body moving through it is a function of the coefficient of drag (C_D), atmospheric density (ρ_{air}) and the velocity of the body (v).

$$\text{Drag } = D = -\frac{1}{2}C_D\rho_{air}Av^2 \tag{2.11}$$

The negative sign indicates that drag acts in the direction opposite to the velocity of the moving body.

$$\Rightarrow \vec{D} = D\cdot\hat{v} \text{ where } \hat{v} = \frac{\vec{v}}{v}$$

Referring to the relationship between the generalized velocities ($\dot{q}_i$) and momenta (p_i) from Section 2.1,

$$\vec{v}_S = \frac{p_r}{m}\hat{r} + \frac{p_\phi}{mr}\hat{\phi} + \frac{p_\theta}{mr\cos\phi}\hat{\theta} \text{ or } \vec{v}_C = \frac{p_x}{m}\hat{i} + \frac{p_y}{m}\hat{j} + \frac{p_z}{m}\hat{k} \tag{2.12}$$

where the subscripts are indicative of the coordinate system.

Using these equations, the components of the drag force are found as:

$$D_r = D\cdot\frac{p_r}{m} \tag{2.13a}$$

$$D_\theta = D\cdot\frac{p_\theta}{mr\cos\phi} \tag{2.13b}$$

$$D_\phi = D \cdot \frac{p_\phi}{mr} \tag{2.13c}$$

$$D_x = D \cdot \frac{p_x}{m} \tag{2.14a}$$

$$D_y = D \cdot \frac{p_y}{m} \tag{2.14b}$$

$$D_z = D \cdot \frac{p_z}{m} \tag{2.14c}$$

2.5 Third-body Perturbations

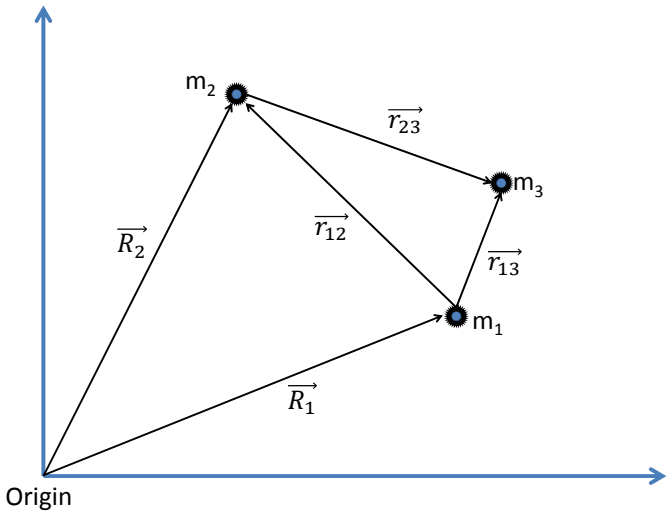

Figure 2.5: Three - body problem

Applying Newton's Gravitational Law to an arbitrary three-body system as shown in Figure 2.5 gives the following equations:

$$m_1 \ddot{\vec{R}}_1 = \frac{Gm_1m_2}{r_{12}^3}\vec{r}_{12} + \frac{Gm_1m_3}{r_{13}^3}\vec{r}_{13}$$

$$m_2 \ddot{\vec{R}}_2 = \frac{Gm_1m_2}{r_{21}^3}\vec{r}_{21} + \frac{Gm_2m_3}{r_{23}^3}\vec{r}_{23}$$

Cancelling m_1 and m_2 on both sides of the first and second equations respectively and then subtracting them yields

$$\ddot{\vec{R}}_2 - \ddot{\vec{R}}_1 = \ddot{\vec{r}}_{12} = -\frac{G(m_1+m_2)}{r_{12}^3}\vec{r}_{12} + Gm_3\left(\frac{\vec{r}_{23}}{r_{23}^3} - \frac{\vec{r}_{13}}{r_{13}^3}\right)$$

Applying this to our Earth-Moon-satellite system where m_2 is negligible,

$$\ddot{\vec{r}} + \frac{\mu_{\oplus}}{r^3}\vec{r} = \mu_{\,\mathbb{D}}\left\{\frac{\vec{r}_{\,\mathbb{D}} - \vec{r}}{|\vec{r}_{\,\mathbb{D}} - \vec{r}|^3} - \frac{\vec{r}_{\,\mathbb{D}}}{|\vec{r}_{\,\mathbb{D}}|^3}\right\} \tag{2.15}$$

The RHS of this equation is considered to be the perturbing force due to Moon's gravitational attraction (M) on the Earth satellite. As stated before, this system is modelled as a two-body problem, where the third-body perturbation is treated as an external force. If the Moon is modelled as a gravitational potential, it then becomes a three-body problem and the ECI coordinate frame will no longer be an inertial one; all of the above calculations will then have to be applied in the Earth-Moon-barycentre frame, making the process tedious, especially for assessing oblateness effects.

As shown in Eq. 2.15, Moon's gravitational perturbations are given by:

$$\vec{M} = \mu_{\,\mathbb{D}}\left\{\frac{\vec{r}_{\,\mathbb{D}} - \vec{r}}{|\vec{r}_{\,\mathbb{D}} - \vec{r}|^3} - \frac{\vec{r}_{\,\mathbb{D}}}{|\vec{r}_{\,\mathbb{D}}|^3}\right\} \tag{2.16}$$

Suppose the Moon makes an angle of γ with the $\hat{i}$-axis as shown in Figure 2.6 and the semi-major axis of its circular orbit is $a_{\,\mathbb{D}}$. Neglecting the angle that the Moon's orbit makes with the ecliptic plane, the position of the moon is

$$\vec{r}_{\,\mathbb{D}} = a_{\,\mathbb{D}}\ \left\{\cos\gamma\ \hat{i} + \cos\epsilon\sin\gamma\ \hat{j} + \sin\epsilon\sin\gamma\ \hat{k}\right\}$$

Referring to Figure 2.1 again, it can be easily seen that

$$\vec{r} = r\ \left[\cos\phi\ \cos\theta\ \hat{i} + \cos\phi\ \sin\theta\ \hat{j} + \sin\phi\ \hat{k}\right]$$

From these two, the quantity $\vec{r}_{\,\mathbb{D}} - \vec{r}$ is found as:

$$\vec{r}_{\,\mathbb{D}} - \vec{r} = a_{\,\mathbb{D}}\ \left\{\cos\gamma\ \hat{i} + \cos\epsilon\sin\gamma\ \hat{j} + \sin\epsilon\sin\gamma\ \hat{k}\right\} - r\ \left\{\cos\phi\cos\theta\ \hat{i} + \cos\phi\sin\theta\ \hat{j} + \sin\phi\ \hat{k}\right\} \tag{2.17}$$

Denoting the components of $\vec{P}$ in Cartesian coordinates by corresponding subscripts:

$$P_x = \vec{P}(1) \tag{2.18a}$$

$$P_y = \vec{P}(2) \tag{2.18b}$$

$$P_z = \vec{P}(3) \tag{2.18c}$$

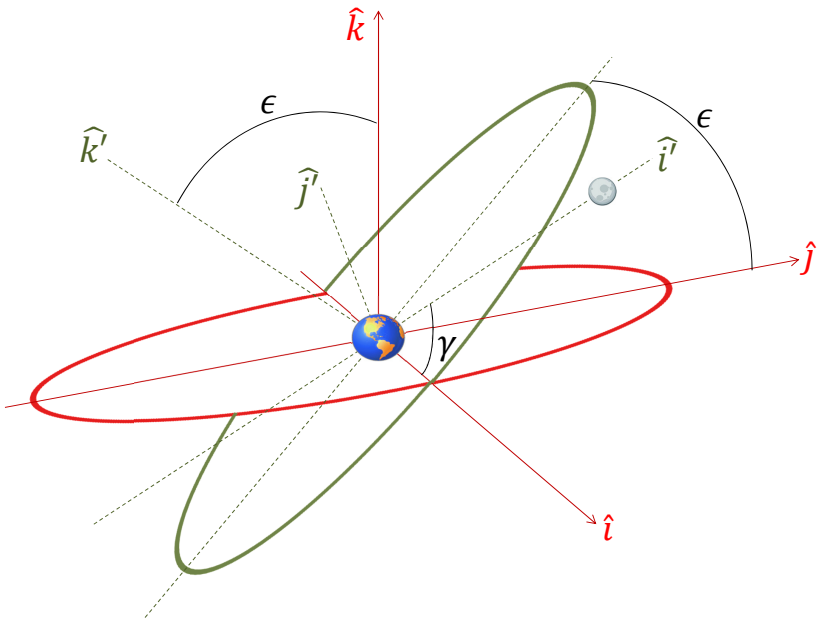

Figure 2.6: Position of the Moon (red = Earth's equatorial plane, green = ecliptic plane)

Components of $\vec{P}$ in spherical coordinates are obtained by using the rotation matrix obtained in Eq. 2.8.

$$P_r = P_x \ \cos\phi \ \cos\theta \ + \ P_y \ \cos\phi \ \sin\theta \ + \ P_z \ \sin\phi \tag{2.19a}$$

$$P_\theta = -P_x \ \sin\theta \ + \ P_y \ \cos\theta \tag{2.19b}$$

$$P_\phi = -P_x \ \sin\phi \ \cos\theta \ - \ P_y \ \sin\phi \ \sin\theta \ + \ P_z \ \cos\phi \tag{2.19c}$$

As with the Sun, $\gamma_{\,\mathbb{D}}$ changes as the Moon goes around the Earth, hence it has to be changed according to $\gamma = \gamma_i + n_{\,\mathbb{D}} t$, where γ_i = initial angle of Moon-line with $\hat{i}$-axis and $n_{\,\mathbb{D}}$ = rate in rad/sec at which the Moon goes around the Earth, assuming circular orbit.

Chapter 3

SOFTWARE DEVELOPMENT

3.1 Overview

MATLAB has been used to numerically solve the ODEs developed in Eq. 2.2 and 2.4. The governing module calls other functions which provide data to continually change the varying parameters in the equations. It also ensures that integration is stopped at the required termination condition and presents the graphical data. The flow of control between submodules is shown in Figure 3.1.

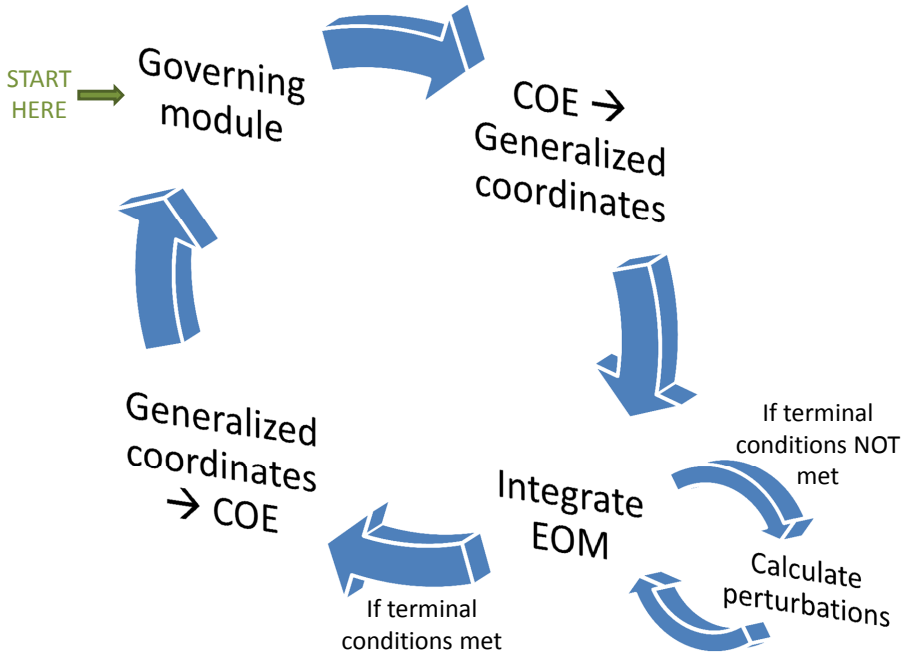

Figure 3.1: Algorithm of the software developed

The solver used, *ode45* implements the Runge-Kutta(4,5) method with a variable step size. Unless mentioned otherwise, a relative tolerance of 3×10^{-14} and an absolute tolerance of 1×10^{-14} is used.

It must be noted that there are TWO governing modules used in this analysis: one that uses Cartesian coordinates and the other that uses spherical coordinates. The following sections will detail the required modules in both software programs. The next chapter will compare the performance of both approaches in detail. They essentially yield exactly the same results; however using Cartesian coordinates eliminates singularities, while using spherical coordinates executes the program faster (provided there are no singularities).

3.2 Conversion between COE and Generalized Coordinates/Momenta

The inputs required are the positional coordinates (r, ϕ, θ OR x, y, z) and momenta (p_r, p_θ, p_ϕ OR p_x, p_y, p_z) of the particle in the base reference frame. But the orbital elements of a spacecraft are usually provided as semi-major axis (a) or perigee height (h_p), true anomaly (f) or eccentric anomaly(M), eccentricity (e), inclination (i), argument of perigee (ω) and ascending node (Ω). Hence, the software should be capable of converting between the three sets.

Eccentric Anomaly to True Anomaly [10]

Input: M, e

Output: f

Given mean anomaly, Kepler's equation is used in conjunction with the Laguerre-Conway iterative method to first find the eccentric anomaly, and then convert that to the true anomaly.

If M = mean anomaly, E = eccentric anomaly and e = eccentricity, then Kepler's equation is given by

$$M = E - e \sin E \tag{3.1}$$

If $F = M - E + e \sin E$, then the Laguerre-Conway algorithm is represented as:

$$E_{i+1} = E_i - \frac{nF(E_i)}{F'(E_i) \pm \sqrt{[(n-1)F'(E_i)]^2 - n(n-1)F(E_i)F''(E_i)}} \tag{3.2}$$

where the first and second derivatives of F are $F'(E_i) = -1 + e\cos(E_i)$ and $F''(E_i) = -e\sin(E_i)$. The order

of the solution, n is chosen arbitrarily to be 4, while the starting value for E is given by

$$E_0 = \frac{M\ [1 - \sin(M+e)] + (M+e)\sin M}{1 + \sin M - \sin(M+e)} \tag{3.3}$$

This algorithm is run to the accuracy of four-decimal points (i.e. 10^{-4}) to obtain the final value of E, which is then converted to f using

$$\tan\left(\frac{E}{2}\right) = \sqrt{\frac{1-e}{1+e}}\tan\left(\frac{f}{2}\right) \tag{3.4}$$

where e = eccentricity, as mentioned earlier.

COE to Generalized Coordinates/Momenta [10]

Input: a (or h_p), f (or M), $e, i, \omega, \Omega, m, \mu_\oplus, R_\oplus$

Output: $(r, p_r, \theta, p_\theta, \phi, p_\phi)$ OR (x, p_x, y, p_y, z, p_z)

Given the classical orbital elements,

$$r = \frac{a(1-e^2)}{1 + e\cos f} = \frac{h_p(1+e)}{1+e\cos f}$$

Then $\vec{r} \equiv\ x\hat{i} + y\hat{j} + z\hat{k}$ can be found in the $\hat{i} - \hat{j} - \hat{k}$ basis as

$$\begin{aligned}\vec{r} = &\ r\ (\cos\Omega\cos(\omega+f) - \sin\Omega\sin(\omega+f)\cos i)\ \hat{i} + \\ &r\ (\sin\Omega\cos(\omega+f) + \cos\Omega\sin(\omega+f)\cos i)\ \hat{j} + \\ &r\ (\sin(\omega+f)\sin i)\ \hat{k}\end{aligned}$$

Therefore, the generalized (Cartesian) coordinates are given by Eq. 3.5:

$$x = r\ (\cos\Omega\cos(\omega+f) - \sin\Omega\sin(\omega+f)\cos i) \tag{3.5a}$$

$$y = r\ (\sin\Omega\cos(\omega+f) + \cos\Omega\sin(\omega+f)\cos i) \tag{3.5b}$$

$$z = r\ (\sin(\omega+f)\sin i) \tag{3.5c}$$

Using Figure 2.1, it is clear that

$$\phi = \tan^{-1}\left(\frac{z}{\sqrt{x^2+y^2}}\right) \text{ and } \theta = \tan^{-1}\left(\frac{y}{x}\right)$$

Therefore, the generalized (spherical) coordinates are given by Eq. 3.6:

$$r = \frac{a(1-e^2)}{1+e\cos f} = \frac{h_p(1+e)}{1+e\cos f} \tag{3.6a}$$

$$\phi = \tan^{-1}\left(\frac{\sin(\omega+f)\sin i}{\sqrt{(\cos\Omega\cos(\omega+f)-\sin\Omega\sin(\omega+f)\cos i)^2+(\sin\Omega\cos(\omega+f)+\cos\Omega\sin(\omega+f)\cos i)^2}}\right) \tag{3.6b}$$

$$\theta = \tan^{-1}\left(\frac{\sin\Omega\cos(\omega+f)+\cos\Omega\sin(\omega+f)\cos i}{\cos\Omega\cos(\omega+f)-\sin\Omega\sin(\omega+f)\cos i}\right) \tag{3.6c}$$

As shown above, the generalized coordinates are easy to find; however a slightly round-about way is required to calculate the corresponding momenta. First the Cartesian components of the velocity are found, then its spherical components calculated using the rotation matrix developed in Eq. 2.8, and finally momenta calculated using Eq. 2.2 - 2.4.

$$\begin{aligned}\vec{v} = & -\sqrt{\frac{\mu_\oplus}{a(1-e^2)}}\ \{\cos\Omega\ [\sin(\omega+f)+e\sin\omega]+\sin\Omega\ [\cos(\omega+f)+e\cos\omega]\cos i\}\hat{i}\ + \\ & -\sqrt{\frac{\mu_\oplus}{a(1-e^2)}}\ \{\sin\Omega\ [\sin(\omega+f)+e\sin\omega]-\cos\Omega\ [\cos(\omega+f)+e\cos\omega]\cos i\}\hat{j}\ + \\ & \sqrt{\frac{\mu_\oplus}{a(1-e^2)}}\ \{[\cos(\omega+f)+e\cos\omega]\sin i\}\hat{k}\end{aligned}$$

$$\begin{aligned}\therefore\ v_x = & -\sqrt{\frac{\mu_\oplus}{a(1-e^2)}}\ \{\cos\Omega\ [\sin(\omega+f)+e\sin\omega]+\sin\Omega\ [\cos(\omega+f)+e\cos\omega]\cos i\} \\ v_y = & -\sqrt{\frac{\mu_\oplus}{a(1-e^2)}}\ \{\sin\Omega\ [\sin(\omega+f)+e\sin\omega]-\cos\Omega\ [\cos(\omega+f)+e\cos\omega]\cos i\} \\ v_z = & \sqrt{\frac{\mu_\oplus}{a(1-e^2)}}\ \{[\cos(\omega+f)+e\cos\omega]\sin i\}\end{aligned}$$

Applying the rotation matrix between $\hat{i}-\hat{j}-\hat{k}$ and $\hat{r}-\hat{\theta}-\hat{\phi}$ from Eq. 2.8,

$$\begin{bmatrix}\hat{i}\\ \hat{j}\\ \hat{k}\end{bmatrix} = \begin{bmatrix}\cos\phi\ \cos\theta & -\sin\theta & -\sin\phi\ \cos\theta\\ \cos\phi\ \sin\theta & \cos\theta & -\sin\phi\ \sin\theta\\ \sin\phi & 0 & \cos\phi\end{bmatrix}\begin{bmatrix}\hat{r}\\ \hat{\theta}\\ \hat{\phi}\end{bmatrix} \tag{2.8}$$

$$
\begin{aligned}
\vec{v} &= v_x\hat{i} + v_y\hat{j} + v_z\hat{k} \\
&= v_x(\cos\phi\ \cos\theta\ \hat{r} - \sin\theta\ \hat{\theta} - \sin\phi\ \cos\theta\ \hat{\phi}) + \\
&\quad v_y(\cos\phi\ \sin\theta\ \hat{r} + \cos\theta\ \hat{\theta} - \sin\phi\ \sin\theta\ \hat{\phi}) + \\
&\quad v_z(\sin\phi\ \hat{r} + \cos\phi\ \hat{\phi})
\end{aligned}
$$

$$
\left.
\begin{aligned}
\Rightarrow \vec{v} = \quad & (v_x\cos\phi\ \cos\theta + v_y\cos\phi\ \sin\theta + v_z\sin\phi)\hat{r} + \\
& (-v_x\sin\theta + v_y\cos\theta)\hat{\theta} + \\
& (-v_x\sin\phi\ \cos\theta - v_y\sin\phi\ \sin\theta + v_z\cos\phi)\hat{\phi}
\end{aligned}
\right\} \equiv (\dot{r})\hat{r} + (r\ \cos\phi\ \dot{\theta})\hat{\theta} + (r\dot{\phi})\hat{\phi}
$$

By comparing the terms on both sides, the velocities in each direction can be calculated:

$$\therefore\ v_r = \dot{r} = v_x\cos\phi\cos\theta + v_y\cos\phi\sin\theta + v_z\sin\phi$$

$$v_\theta = r\cos\phi\ \dot{\theta} = -v_x\sin\theta + v_y\cos\theta$$

$$v_\phi = r\dot{\phi} = -v_x\sin\phi\cos\theta - v_y\sin\phi\sin\theta + v_z\cos\phi$$

Now that all the components of the velocity are known, generalized momenta are obtained using Eq. 3.7 - 3.8.

$$p_x = mv_x = -\sqrt{\frac{\mu_\oplus m^2}{a(1-e^2)}}\ \{\cos\Omega\ [\sin(\omega+f) + e\sin\omega] + \sin\Omega\ [\cos(\omega+f) + e\cos\omega]\cos i\} \tag{3.7a}$$

$$p_y = mv_y = -\sqrt{\frac{\mu_\oplus m^2}{a(1-e^2)}}\ \{\sin\Omega\ [\sin(\omega+f) + e\sin\omega] - \cos\Omega\ [\cos(\omega+f) + e\cos\omega]\cos i\} \tag{3.7b}$$

$$p_z = mv_z = \sqrt{\frac{\mu_\oplus m^2}{a(1-e^2)}}\ \{[\cos(\omega+f) + e\cos\omega]\sin i\} \tag{3.7c}$$

$$p_r = mv_r = m(v_x\cos\phi\ \cos\theta + v_y\cos\phi\ \sin\theta + v_z\sin\phi) \tag{3.8a}$$

$$p_\theta = mr\cos\phi\ v_\theta = mr\cos\phi(-v_x\sin\theta + v_y\cos\theta) \tag{3.8b}$$

$$p_\phi = mrv_\phi = mr(-v_x\sin\phi\ \cos\theta - v_y\sin\phi\ \sin\theta + v_z\cos\phi) \tag{3.8c}$$

Generalized Coordinates/Momenta to COE [10]

Input: $(r, p_r, \phi, p_\phi, \theta, p_\theta, m, \mu_\oplus, R_\oplus)$ OR $(x, p_x, y, p_y, z, p_z, m, \mu_\oplus, R_\oplus)$

Output: $f, a, h_p, e, i, \omega, \Omega$

Since $\vec{r}$ and $\vec{v}$ are known, the following procedure can be used to find the individual orbital elements [10]:

$$e = |\vec{e}| = \left| \left(\frac{v^2}{\mu_\oplus} - \frac{1}{r} \right) \vec{r} - \frac{(\vec{r} \cdot \vec{v})\vec{v}}{\mu_\oplus} \right| \tag{3.9}$$

$$\cos f = \frac{\vec{r} \cdot \vec{e}}{re} \tag{3.10}$$

Quadrant ambiguity is resolved by checking for $0 \leq f \leq \pi$ if $\vec{r} \cdot \vec{v} \geq 0$, or $\pi < f < 2\pi$ if $\vec{r} \cdot \vec{v} < 0$.

Before proceeding, the following quantities are needed from Eq. 2.8 in case the given $\vec{r}$ and $\vec{v}$ are in spherical coordinates:

$$\hat{i} = \cos\phi \cos\theta \; \hat{r} - \sin\theta \; \hat{\theta} - \sin\phi \cos\theta \; \hat{\phi}$$

$$\hat{k} = \sin\phi \; \hat{r} + \cos\phi \; \hat{\phi}$$

These above expressions can be utilized to find the rest of the classical orbital elements:

$$\cos i = \frac{\vec{h} \cdot \hat{k}}{h} = \frac{h_z}{h} \tag{3.11}$$

where $\vec{h}$ is the angular momentum vector defined by $\vec{h} = \vec{r} \times \vec{v}$. This equation gives the value of inclination such that $0 \leq i \leq \pi$; if $\pi < i < 2\pi$, it means that the orbit is retrograde and such orbits have not been considered.

Other quantities need a *nodal vector* to be defined:

$$\vec{n} = \hat{k} \times \frac{\vec{h}}{h}$$

$$\cos\Omega = \frac{\vec{n} \cdot \hat{i}}{n} = \frac{n_x}{n} \tag{3.12}$$

Again the the correct quadrant of Ω is obtained from the condition that $0 \leq \Omega \leq \pi$ if $\vec{n} \cdot \hat{J} = n_y \geq 0$, or $\pi < \Omega < 2\pi$ if $n_y < 0$.

$$\cos\omega = \frac{\vec{n} \cdot \vec{e}}{ne} \tag{3.13}$$

where $0 \leq \omega \leq \pi$ if $\vec{e} \cdot \hat{k} = e_z \geq 0$, and $\pi < \omega < 2\pi$ if $e_z < 0$.

3.3 Calculation of $\mathbf{F}_{SRP}$

There are only two values that the magnitude of this force can take:

$$F_{SRP} = \begin{cases} 8.208 \times 10^{-3} \cdot A & \text{if in sunlight} \\ 0 & \text{if in Earth's shadow} \end{cases} \tag{3.14}$$

where A = area exposed to sunlight (in km^2). The conditions for shadow (Section 2.2) are checked every time step and the corresponding value of F_{SRP} implemented. Then Eq. 2.6a and 2.9 are used to update the Cartesian or spherical components of SRP.

To account for the change in the position of the Sun, an additional ODE is appended to the original set of EOM in Eq. 2.4 and 2.4:

$$\dot{\lambda} = -1.99097 \times 10^{-7} \text{ rad/sec} \tag{3.15}$$

where λ is the angle that the Sun-line makes with $\hat{i}$ of the reference ECI frame as shown in Figure 2.3.

3.4 Calculation of Drag

Input:	$r, p_r, \phi, p_\phi, p_\theta, m, A, R_\oplus$	Output:	D_r, D_ϕ, D_θ
OR			
Input:	$x, p_x, y, p_y, z, p_z, m, A, R_\oplus$	Output:	D_x, D_y, D_z

In this program, an exponential model is implemented to calculate the atmospheric density, i.e. the density of air ρ at height h is given by [3]

$$\rho = \rho_0 e^{-(h-h_0)/H}$$

where ρ_0 = reference atmospheric density at the reference height h_0 and H = scale height.

The set of 28 reference heights shown in Table 3.1 reproduced from Reference [3], encompassing altitudes from 25 km to 1000 km, is hard-coded into the program. The same reference height is used for all altitudes greater than 1000 km.

At every time step, the value of the atmospheric density is updated based on the numerically integrated values of the input parameters. Then Eq. 2.14 and 2.13 are used to update the Cartesian or spherical components of drag force.

Table 3.1: Various reference heights used for the implemented exponential atmospheric model [3]

	Altitude (km)	Reference height (km)	Scale height (km)	Atmospheric density (kg/m^3)
1	0-25	0	7.249	1.225
2	25-30	25	6.349	$3.899\text{x}10^{-2}$
3	30-40	30	6.682	$1.774\text{x}10^{-2}$
4	40-50	40	7.554	$3.972\text{x}10^{-3}$
5	50-60	50	8.382	$1.057\text{x}10^{-3}$
6	60-70	60	7.714	$3.206\text{x}10^{-4}$
7	70-80	70	6.549	$8.770\text{x}10^{-5}$
8	80-90	80	5.799	$1.905\text{x}10^{-5}$
9	90-100	90	5.382	3.39610^{-6}
10	100-110	100	5.877	$5.297\text{x}10^{-7}$
11	110-120	110	7.263	$9.661\text{x}10^{-8}$
12	120-130	120	9.473	$2.438\text{x}10^{-8}$
13	130-140	130	12.636	$8.484\text{x}10^{-9}$
14	140-150	140	16.149	$3.845\text{x}10^{-9}$
15	150-180	150	22.523	$2.070\text{x}10^{-9}$
16	180-200	180	29.740	$5.464\text{x}10^{-10}$
17	200-250	200	37.105	$2.789\text{x}10^{-10}$
18	250-300	250	45.546	$7.248\text{x}10^{-11}$
19	300-350	300	53.628	$2.418\text{x}10^{-11}$
20	350-400	350	53.298	$9.518\text{x}10^{-12}$
21	400-450	400	58.515	$3.725\text{x}10^{-12}$
22	450-500	450	60.828	$1.585\text{x}10^{-12}$
23	500-600	500	63.822	$6.967\text{x}10^{-13}$
24	600-700	600	71.835	$1.454\text{x}10^{-13}$
25	700-800	700	88.667	$3.614\text{x}10^{-14}$
26	800-900	800	124.64	$1.170\text{x}10^{-14}$
27	900-1000	900	181.05	$5.245\text{x}10^{-15}$
28	>1000	1000	268.00	$3.019\text{x}10^{-15}$

3.5 Calculation of Moon's Perturbations

Third-body gravitational perturbation by the Earth's Moon is accounted for by using Eq. 2.18 or 2.19. The final ODE to be solved simultaneously with Eq. 2.2 or 2.4 and Eq. 3.15 is the one that accounts for the movement of the Moon:

$$\dot{\gamma} = 2.6491 \times 10^{-6} \text{ rad/sec} \tag{3.16}$$

where γ is the angle that the Moon-line makes with $\hat{i}$ of the reference ECI frame as shown in Figure 2.6. This differential equation is used to update the position of the Moon at every time step, which is then fed into Eq 2.15-2.19.

Chapter 4

VALIDATION OF MODEL

4.1 Cartesian coordinates vs. Spherical coordinates

As iterated hitherto, *two* governing modules have been developed - the spherical coordinate module (SCM) and the Cartesian coordinate module (CCM). In this section, they have been compared with each other for accuracy (with respect to each other) and speed. Only two tests are conducted to check for these characteristics, since the same algorithm and formulation is coded into both. Tables 4.1 and 4.2 show the results obtained from both modules when started from the same initial conditions – $f = 0°$, $h_p = 662.8249$ km, $e = 0.12479$, $i = \Omega = \lambda = \gamma = 0°$ and $\omega = 110.5464°$. These specific initial conditions are chosen because they are identical to the ones used in Section 4.2. The condition for termination of orbital propagation in both modules is $h_p \leq 250$ km. In Table 4.1, only the effects of SRP and drag are tested for, while all four perturbations (SRP, drag, J_2 and Moon's attraction) are turned on in Table 4.2.

Table 4.1: Comparison of modules while only SRP and drag perturbations are turned on

	SCM	CCM
Orbital lifetime	46.9294 days	46.9294 days
Time taken for code to terminate	638.965938 seconds	1159.401254 seconds

Table 4.2: Comparison of modules while SRP, drag, J_2 and Moon's attractive perturbations are turned on

	SCM	CCM
Orbital lifetime	28.1481 days	28.1481 days
Time taken for code to terminate	414.622320 seconds	815.773137 seconds

It is recognised that the SCM does suffer from singularities if the orbit to be simulated is such that $\sin\phi = 0$. Although the use of Cartesian coordinates eliminates singularities, as the above tables show, the CCM runs slower than the SCM. Hence, the SCM is employed for the remaining tests in this chapter, used for validation of the model developed.

4.2 Solar Radiation Pressure and Drag

The work of Colombo et. al [1] has a similar set-up as in the present analysis and is used here to validate the results. The characteristics of both models are compared in Table 4.3.

Table 4.3: Comparison between models developed in SCM and by Colombo et. al [1]

Characteristics	Colombo et. al [1]	SCM
Orbits considered	Ecliptic only	No specific choice
Perturbations included	SRP and Drag	SRP, Drag, J_2 and Moon's attraction
Exponential atmospheric model	Only one reference height	28 reference heights
Direction of Sun's rotation	Counterclockwise	Clockwise
Equations integrated	Gauss' orbital equations	Hamiltonian equations
Direction of Sun's rotation	Counterclockwise	Clockwise

The direction of change of $\lambda_{\odot}$ is deduced to be counterclock wise because the Earth orbits the Sun in a clockwise manner. The obliquity of the ecliptic has also been taken in to consideration while deriving the EOM. However, the purpose of this section is to validate the current model by comparing it to the work of Colombo et. al [1]; hence, the same conditions as in this reference are used in the first test.

Figures 4.1 - 4.3 show the performance of SCM; they can be compared with the results in Reference [1].

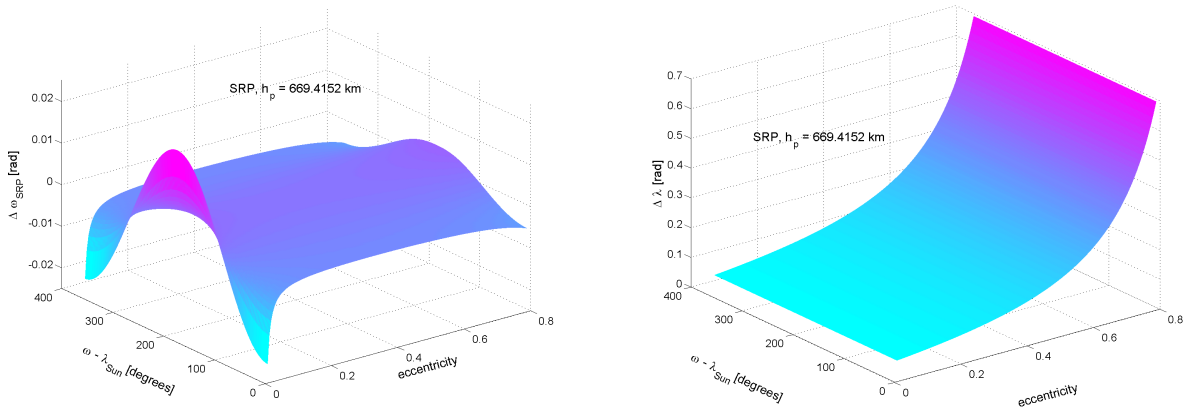

(a) (b)

Figure 4.1: Variation of argument of perigee over single orbit due to SRP and Sun-line precession as a function of initial condition in eccentricity and $\omega - \lambda_{Sun}$ at $h_p = 669.4152$ km; (a) change in ω due to SRP (b) Sun-line precession.

The profiles of change of classical orbital elements (a, e, ω, λ) over one orbit as a function of initial $\omega - \lambda_{\odot}$ and eccentricity generated by SCM are identical to those in Reference [1]. The physical significance of the angle $\omega - \lambda_{\odot}$ is as follows: when $\omega - \lambda_{\odot} = 0$, the perigee and the Sun are on opposite sides of the Earth, while at $\omega - \lambda_{\odot} = \pi$, they are both on the same side of the Earth. The initial condition for $\omega - \lambda_{\odot}$ is achieved by arbitrarily setting $\lambda = 0$.

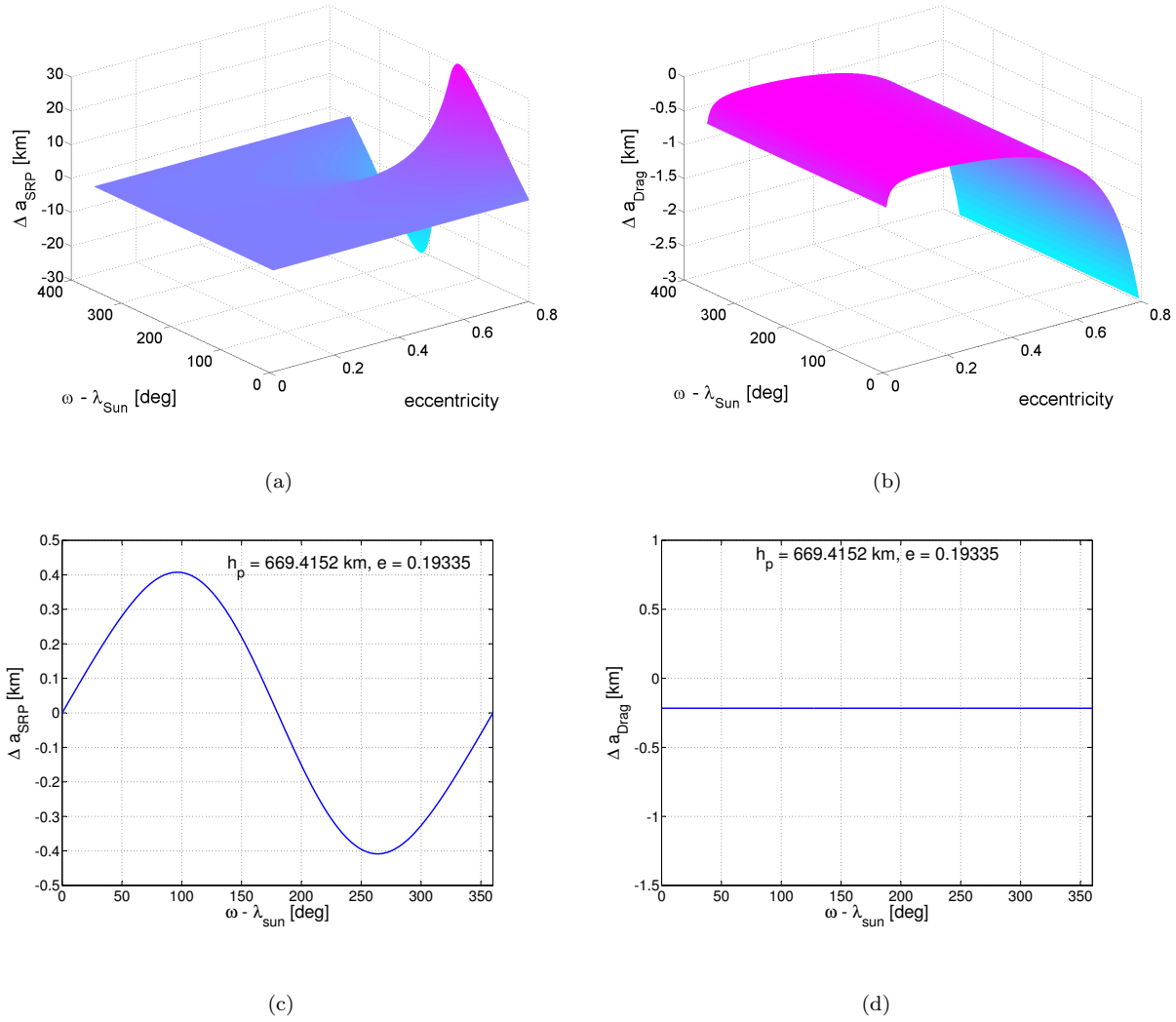

Figure 4.2: Variation of semi-major axis over single orbit as a function of initial condition in eccentricity and $\omega - \lambda_{Sun}$ with initial condition of $h_p = 669.4152$ km (a) due to drag, (b) due to SRP (c) cross-section of Δa_{SRP} at $e = 0.19335$ (d) cross-section of Δa_{Drag} at $e = 0.19335$.

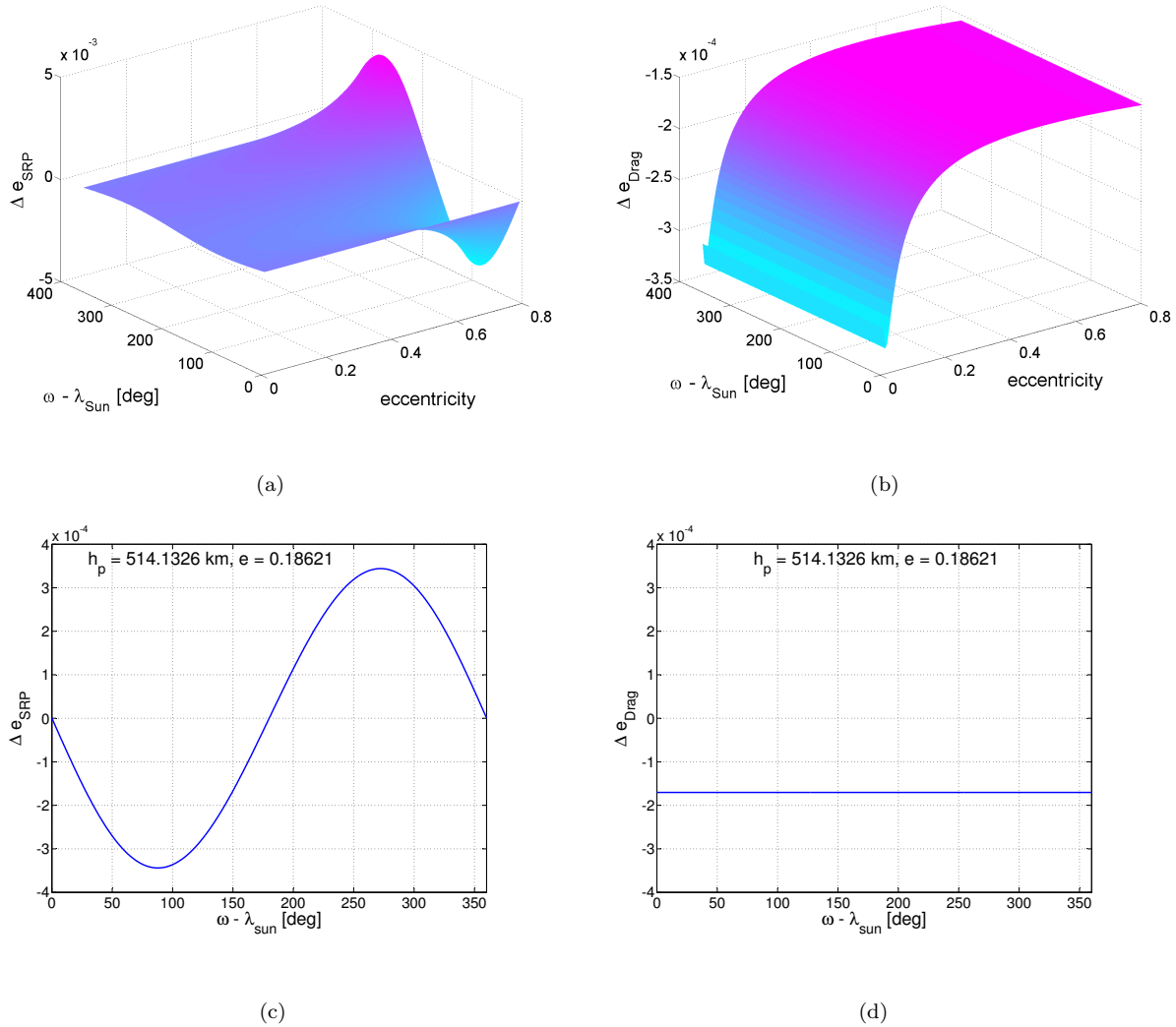

Figure 4.3: Variation of eccentricity over single orbit as a function of initial condition in eccentricity and $\omega - \lambda_{Sun}$ with initial condition of $h_p = 514.1326$ km (a) due to drag, (b) due to SRP (c) cross-section of Δe_{SRP} at $e = 0.18621$ (d) cross-section of Δe_{Drag} at $e = 0.18621$.

A particular case study has been presented by Colombo et. al, estimating the lifetime of a satellite with $A/m = 32.6087$ m^2/kg and $C_D = 2.1$, under effect of drag and SRP. Table 4.4 provides a comparison between results obtained from both sources (reference and SCM) by starting from the same set of initial conditions: $e = 0.12479$, $h_p = 662.8249$ km, $\omega - \lambda_{Sun} = 110.5464°$. At this point in testing, J_2 and Moon's perturbations are turned off in SCM and an orbit lying only in the ecliptic plane is considered.

Table 4.4: Comparison between results obtained in Reference [1] and from SCM by starting from the same set of initial conditions for estimating lifetime of satellite under effect of drag and SRP.

	Test	Orbital lifetime
1	Colombo et. al [1]	47.759 days
2	SCM - Same atmospheric model and CCW rotation of Sun (results shown in Figure 4.4)	47.7384 days
3	Better atmospheric model (exponential with 28 ref. heights) and CCW rotation of Sun	46.6875 days
4	Better atmospheric model and CW rotation of Sun	39.6655 days

Only the first and the second result in the above table are comparable, since they have been calculated under identical conditions. Also, the profile of change in perigee height over the orbital lifetime obtained as Figure 4.4 is identical to Figure 15 of Reference [1]. This also verifies the formulation developed and coded in SCM (and by extension, in the CCM). Thus the fidelity of the model with respect to predicting the effects of SRP and drag is verified by comparing the results to those found in existing literature.

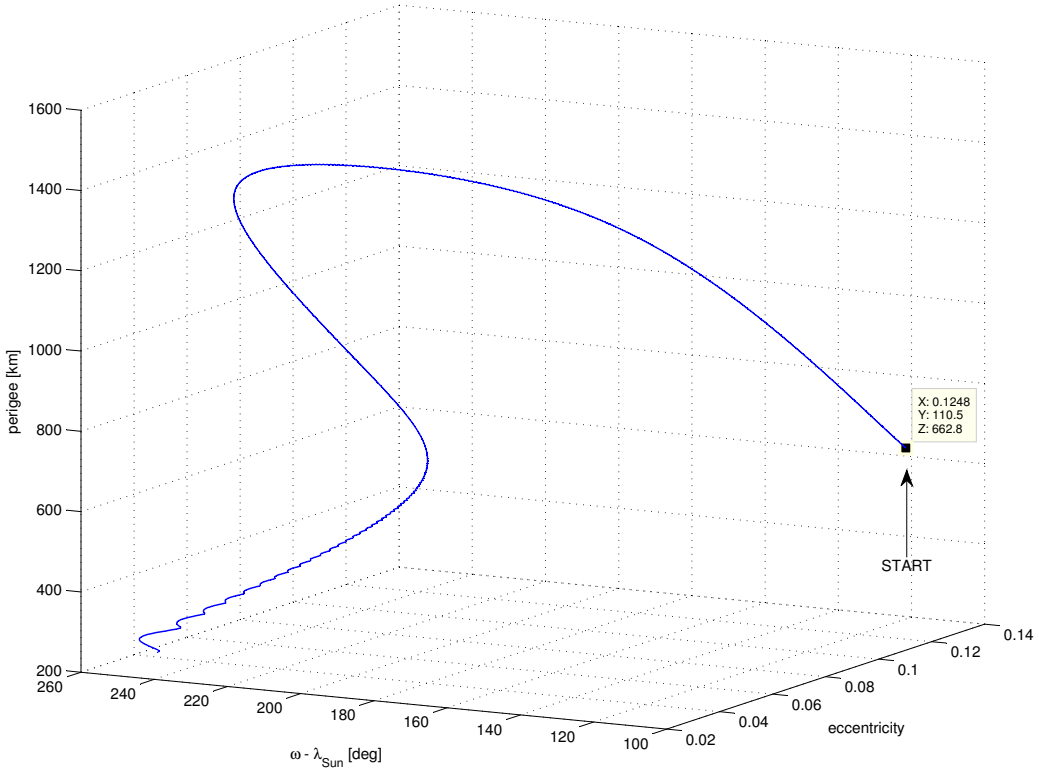

Figure 4.4: Profile of change in perigee height over the satellite's lifetime for $A/m = 32.6087$ m^2/kg. Initial conditions - $e = 0.12479$, $h_p = 662.8249$ km, $i = 0°$, $\omega - \lambda_{Sun} = 110.5464°$.

4.3 Earth Oblateness (J_2)

Launched in 1958, Vanguard was the fourth artificial Earth satellite. The average effect of Earth's J_2 on Vanguard is documented in the Handbook of Orbital Perturbations [11]. Three sample initial COE of Vanguard [12] are propagated using the SCM and the results compared with the predicted average change given in the handbook.

The code is propagated through 30 days and the secular change in ω and Ω is fit using a linear curve through the output data. This linear fitting is conducted to obtain the average effect, as opposed to non-secular effect given by SCM, in order to rightfully compare with the data in the aforementioned handbook.

Table 4.3 shows the result of the above exercise - the first row consists of values from literature, while the next three rows contain data obtained from SCM. The reader can notice that that results from SCM almost match those given by Blitzer [11].

Table 4.5: Comparison of $\dot{\omega}$ and $\dot{\Omega}$ from literature and code.

	Initial conditions	$\dot{\omega}$ $[^\circ/day]$	$\dot{\Omega}$ $[^\circ/day]$
1	Blitzer [11] $a = 1.3603R_e,\ e = 0.1896,\ i = 34.26^\circ$	4.41	-3.02
2	$a = 1.36192R_e,\ e = 0.19068,\ i = 0.59755$ rad, $\omega = 2.9307$ rad, $\Omega = 2.2138$ rad, $M = 3.29021$ rad [12] (Figure 4.5 and Figure 4.6)	4.4109	-3.015
3	$a = 1.36191R_e,\ e = 0.19044,\ i = 0.59783$ rad, $\omega = 3.3911$ rad, $\Omega = 1.8985$ rad, $M = 5.42354$ rad [12]	4.4034	-3.0115
4	$a = 1.36094R_e,\ e = 0.18993,\ i = 0.59786$ rad, $\omega = 6.2191$ rad, $\Omega = 5.9131$ rad, $M = 5.42354$ rad [12]	...	-3.0156

Figure 4.5 shows this process in detail, with initial conditions as mentioned in Table 4.3. The blue line shows the instantaneous change in ω and Ω for thirty days. The red line represents the linear fit. The equation of linear fitting is also displayed. Figure 4.6 shows a zoomed-in version of Figure 4.5, where the same data is plotted and fit for just one day of simulation time. It elucidates more clearly the trend in the change of ω and Ω.

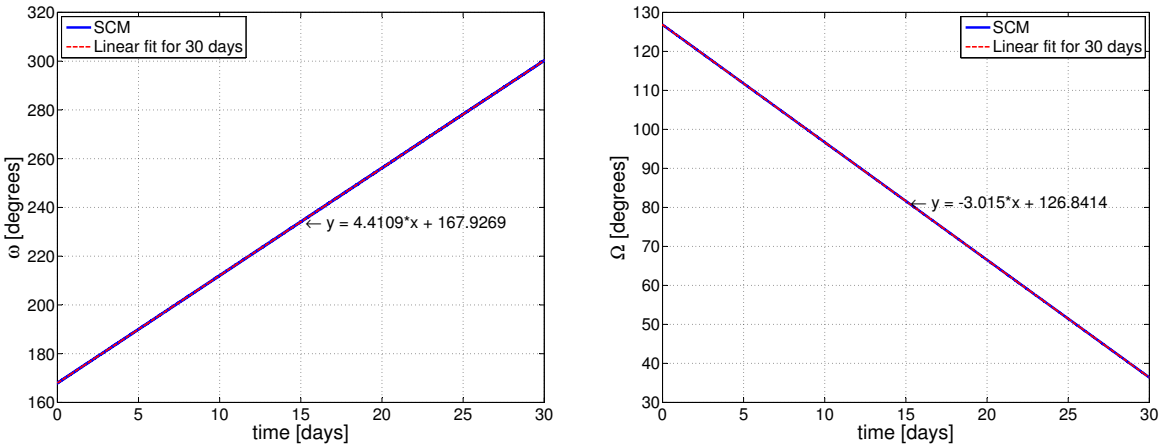

(a) (b)

Figure 4.5: Change in argument of perigee and ascending node over 30 days due to J_2 only (a) ω (b) Ω.

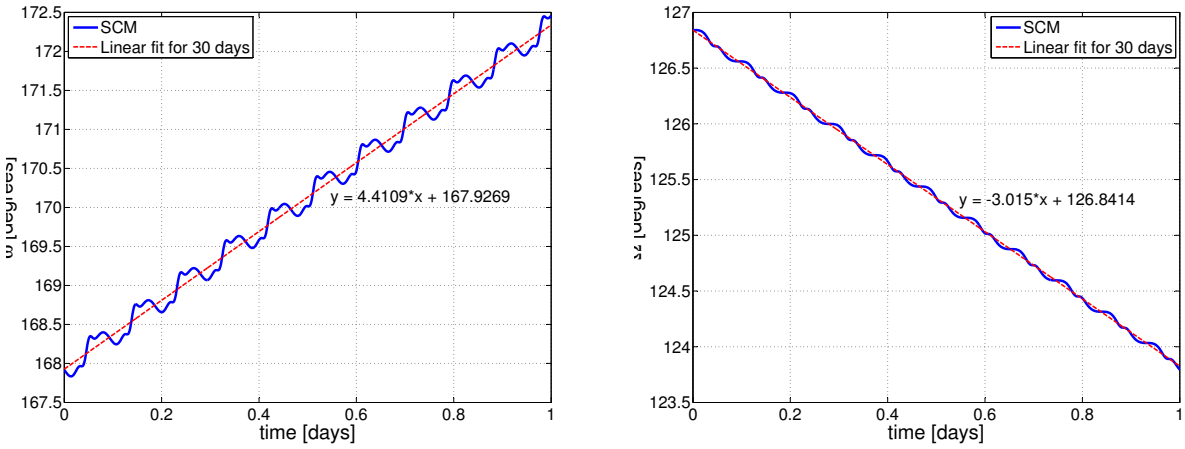

(a) (b)

Figure 4.6: Change in argument of perigee and ascending node over 1 day due to J_2 only (a) ω (b) Ω.

4.4 Moon's Gravitational Perturbations

Lane [2] contrasts two analytical methods of assessing Moon's perturbations in terms of numerical error each method would incorporate. Figure 4.7 in this paper shows the lunar perturbation of the semi-major axis of a GEO sync satellite with initial conditions $a = 42164.1$ km, $e = 0.001$, $i = 1.5°$, $\omega = 145°$, $\Omega = 166°$ and $M = 25.413°$, where the Lagrange equations have been directly integrated. This reference only contains graphical information, hence numbers cannot be provided for comparison between results in the paper and SCM. The main issue that exists with testing this part of the code is that the initial conditions of any Earth satellite orbit never include the angle it makes with the Moon, which is an essential piece of information for SCM and CCM. Hence this angle (i.e. γ from Figure 2.6) has been estimated using trial and error until the graphical results from the reference approximately match those from SCM. This is the procedure of the first test conducted to check the modelling of Moons perturbations.

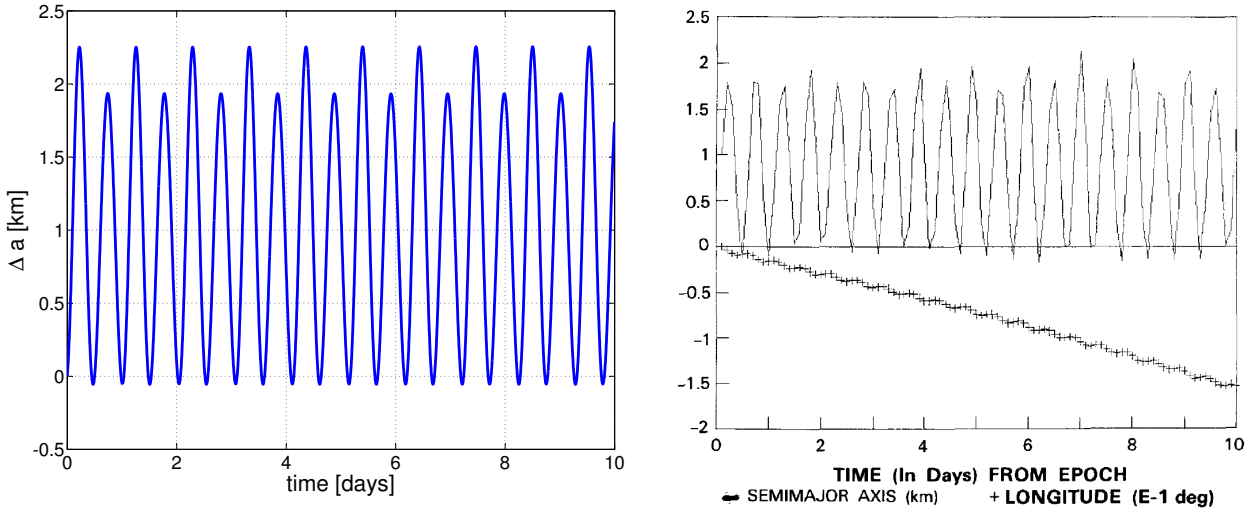

(a) (b)

Figure 4.7: Lunar perturbation of semi-major axis. Initial conditions are $a = 42164.1$ km, $e = 0.001$, $i = 1.5°$, $\omega = 145°$, $\Omega = 166°$ and $\gamma = 45°$. (a) Results from SCM (b) Results from Lane [2]

Figure 4.7 shows that the use of same initial conditions in SCM as those in [2] produce visually similar results. However, due to the trial-and-error nature of this test, another internal check is conducted to understand the behaviour of the SCM. This is explained in the next section.

4.4.1 Example 1: Lagrange points

Third-body perturbations have been modelled in this study as a force, not as a potential, i.e. not included in the Hamiltonian function of the system, but instead added on the RHS of the equations of motion. This means that this entire system is treated as a two-body problem, rather than a three-body problem. The underlying assumption is that both approaches are equivalent, and if the value of the force can be calculated and changed at every time step that the integrator takes, then the results from both approaches should display the same behaviour. Hence, for this section and the next, a special module has been written which numerically solves the three-body problem, whose results can then be compared with those from SCM under similar conditions of propagation. This new program considers only the gravitational interactions between the three-bodies.

Lagrange points are the five positions in a circularly restricted three-body problem where the body of negligible mass will remain stationary with respect to the other two (massive) bodies. It can be theoretically shown that the positions L_4 and L_5 are stable, whereas L_1, L_2 and L_3 are not.

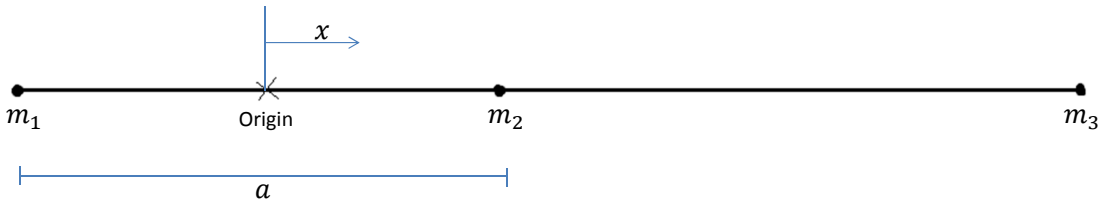

Figure 4.8: Circularly restricted three-body problem

The origin of the reference axis for calculating the Lagrange points is the center of mass (COM) of the system. Now let

$$\chi = \frac{x_3 - x_2}{a}$$

where x_2 and x_3 are the distances of m_2 and m_3 respectively from the origin as shown in Figure 4.8, then the Lagrange points are given by the equation:

$$m_1\chi^5 + 3m_1\chi^4 + 3m_1\chi^3 - 3m_3\chi^2 - 3m_3\chi - m_3 = 0$$

where m_1 and m_3 are relative masses of the bodies.

For the Earth-Moon system, $m_1 = 0.98785$ and $m_2 = 0.01215$. The distance between them $a = 1$ is used,

to reduce everything to canonical units. This gives χ to be $= 0.177768$, thereby placing L_1 at a distance of $\frac{a}{(\chi+1)} - m_1 a$ from the origin. L_4, on the other hand, lies at the same distance as the Moon, just ahead of it by 60°.

Now both codes are run for L_1 and L_4 for 100 orbits and the results are compared to see how much the orbit of the Earth-satellite differs or matches. Results are presented in Figure 4.9 and 4.13. To evaluate the model developed in this analysis, it is more appropriate to compare the phase diagrams from both approaches (Figure 4.10 - 4.12 show them for the L_1 point). The dissimilarities in the phase diagrams arise due to the different coordinate systems used; its the shape of these diagrams that should be compared. These differences can be accounted by remembering that the value of r calculated in both coordinate frames will differ, which will in turn effect the magnitudes of p_θ and p_ϕ (refer Eq. 2.2).

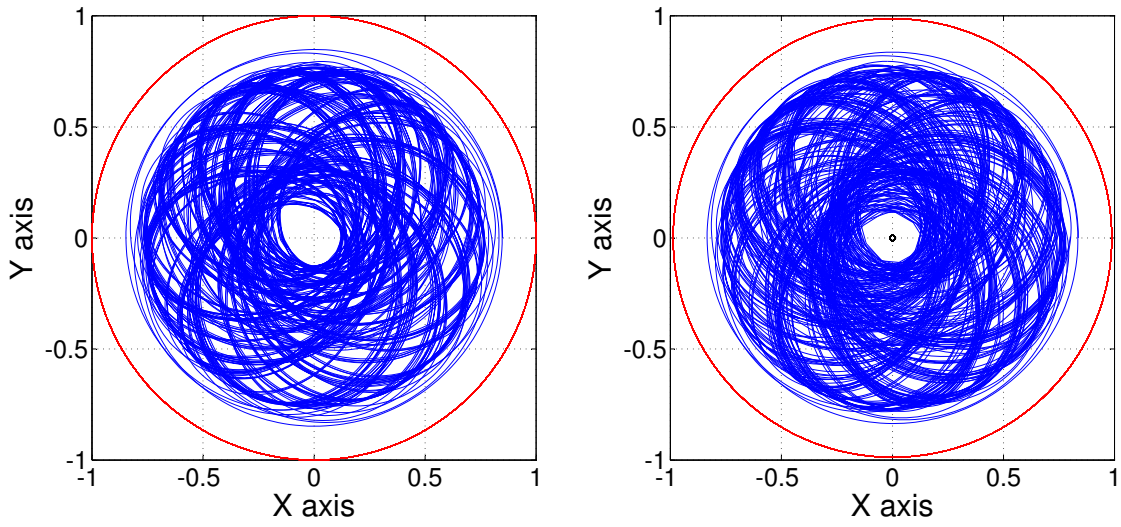

(a) (b)

Figure 4.9: Satellite at L_1 point where third-body perturbations are modelled as (a) force (b) potential. The orbital path/trajectory of the satellite is shown in blue, Moon is red and the rotation of Earth around the Earth-Moon barycentre is in black (only in (b)).

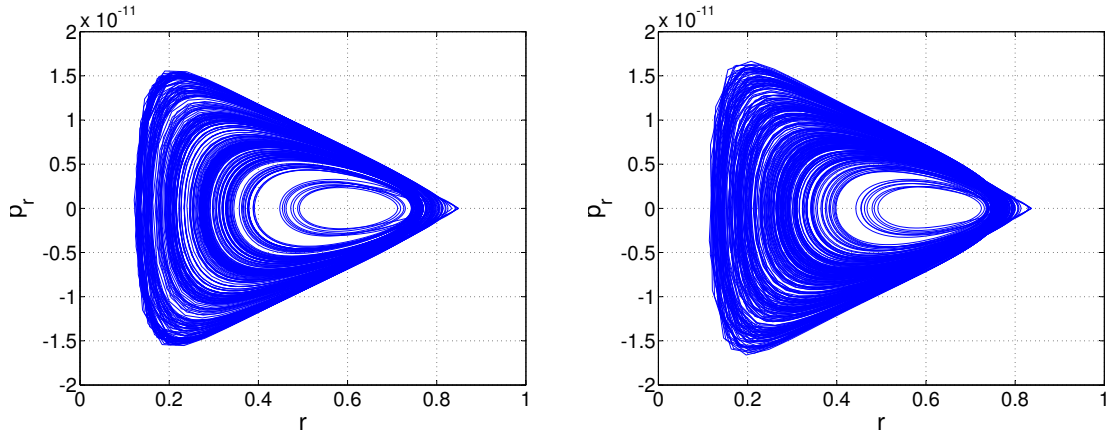

(a) (b)

Figure 4.10: Phase-space plot of p_r vs. r at L_1 point where third-body perturbations are modelled as (a) force (b) potential

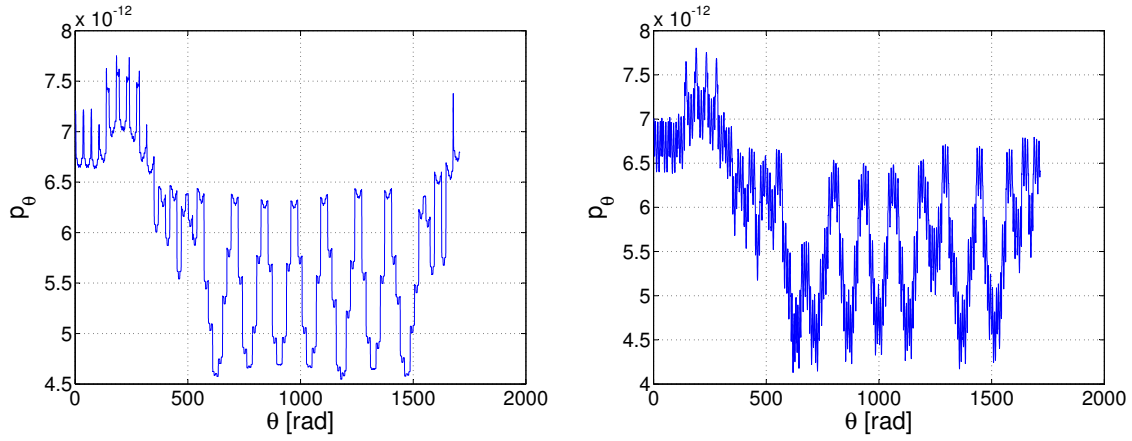

(a) (b)

Figure 4.11: Phase-space plot of p_θ vs. θ at L_1 point where third-body perturbations are modelled as (a) force (b) potential

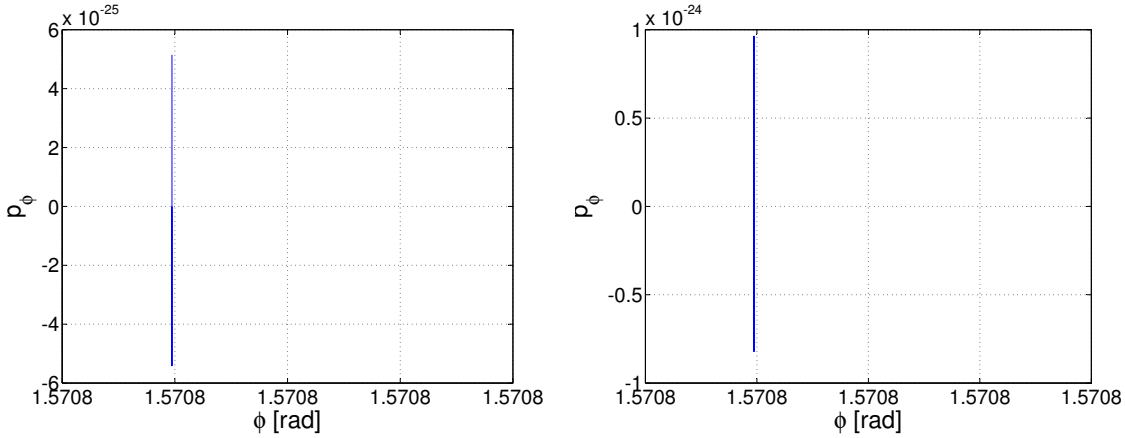

(a) (b)

Figure 4.12: Phase-space plot of p_ϕ vs. ϕ at L_1 point where third-body perturbations are modelled as (a) force (b) potential

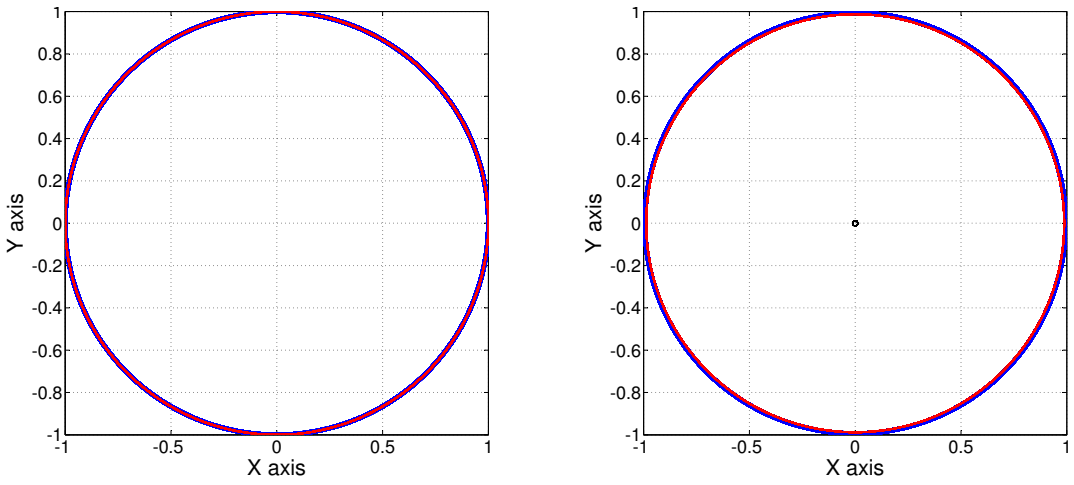

(a) (b)

Figure 4.13: Satellite at L_4 point where third-body perturbations are modelled as (a) force (b) potential. The orbital path/trajectory of the satellite is shown in blue, Moon is red and the rotation of Earth around the Earth-Moon barycentre is in black (only in (b)).

4.4.2 Example 2: Sitnikov Problem

The Sitnikov problem is a form of the restricted three-body problem, where the system consists of two primaries of equal masses, while the third body (referred to as the "satellite") has negligible mass. If the initial positional coordinates of this satellite are such that it only has a non-zero Z-coordinate, where the origin is the barycentre of the system, then the motion of this body is one-dimensional, i.e. it only moves along the Z-axis [13]. This set-up can be used to show that the model developed for estimating third-body perturbations in this analysis is accurate for a certain period of time, until numerical errors build up to unacceptable limits. The Sitnikov solution is extremely sensitive to any velocity (or equivalently, momentum) along any direction. This implies that even small numerical errors will result in deviation from ideal Sitnikov solution [14].

By running the code for the model developed here, it can be shown that the assumption of modelling the third-body perturbation as a force, instead of a potential, holds valid. If the origin of the reference frame is the barycentre, then the particle seems to move up and down along the Z-axis. However, the origin in the frame of reference considered is the center of one of the primaries, which means that the second primary goes around it, as well as the satellite, at the same angular velocity. This is just a slightly different way of looking at the three-body configuration.

The assumption is that the satellite is orbiting the primary, which is located at the origin. This Sitnikov system is extremely susceptible to any error build-up. The very nature of the integrator used here causes error build-up, thus sending the satellite into orbit around one of the massive bodies [14]. Ideal Sitnikov behaviour is seen for a little over two orbits (normalized units) if initial condition of $\phi = \pi/4$ is used and for over ten orbits if initial condition of $\phi = 2\pi/5$ is used. This is because the numerical errors build up and destabilize the system.

Figure 4.14 and Figure 4.18 shows the path of the satellite as propagated by the code (in the case of starting at $\phi = 2\pi/5$). The initial condition of $\gamma = \theta = 0$ is input for both starting points, i.e. the line joining the origin and the satellite also goes through the second primary at the very beginning of the simulation.

A deeper understanding of any problem comes from the phase diagrams. These are shown in Figures 4.15 - 4.17 and Figures 4.19 - 4.21. Since gravitational forces are conservative, the $r - p_r$ and $\phi - p_\phi$ phase diagrams consist of closed shapes. It can be seen from these phase diagrams that ideal Sitnikov behaviour persists until the numerical errors add up, thereby destabilizing the system.

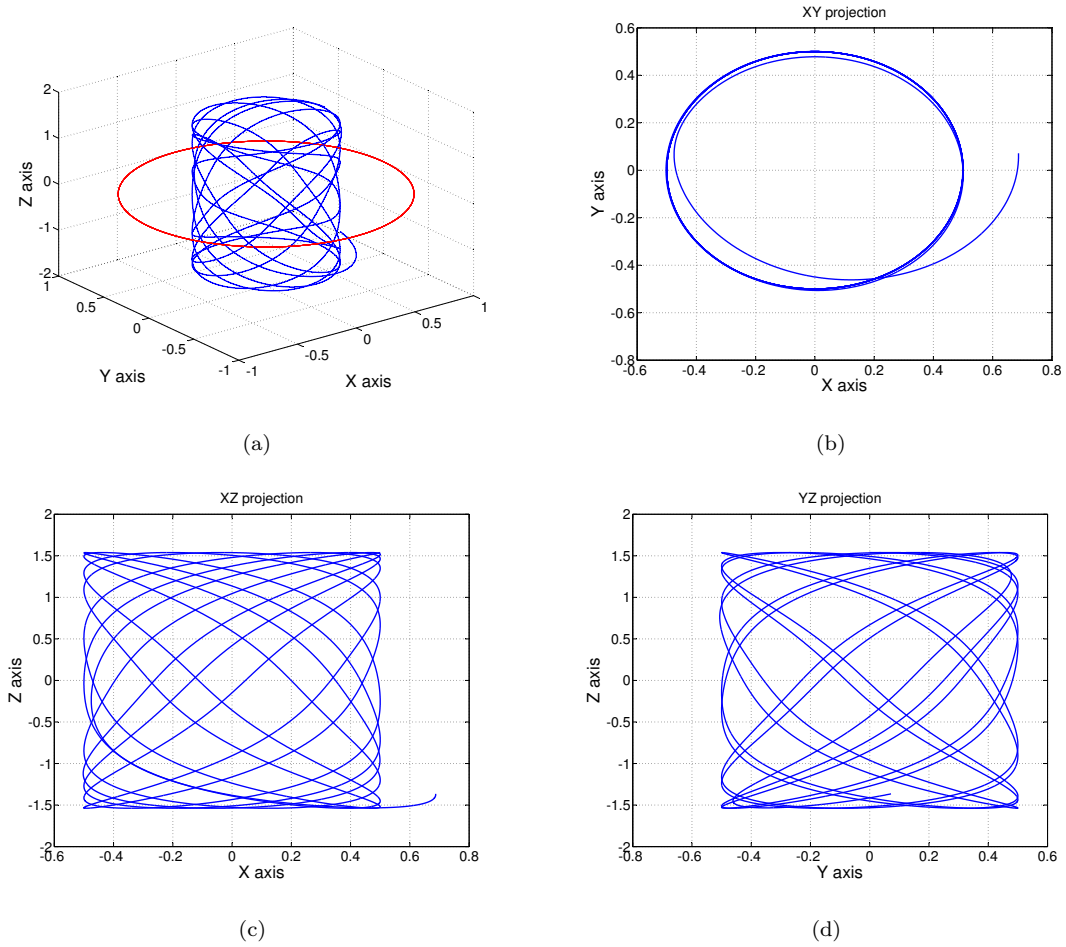

(a) (b)

(c) (d)

Figure 4.14: Simulation of the Sitnikov problem when started from $\phi = 2\pi/5$ and run for 12 orbits. The red circle in the first figure represents the motion of the second primary body about the first. (a) 3D view (b) X-Y view (c) X-Z view (d) Y-Z view

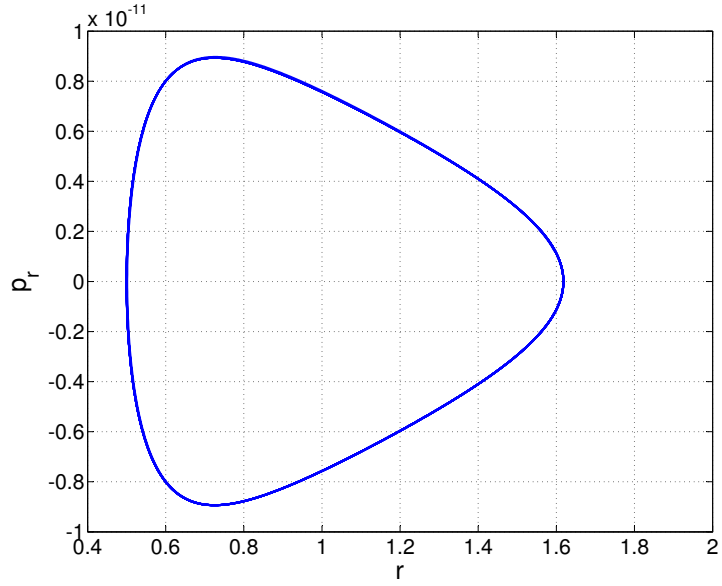

(a)

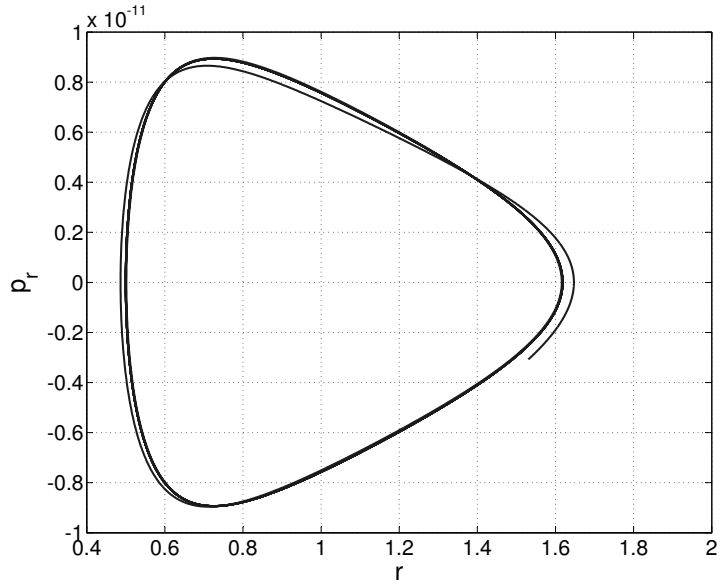

(b)

Figure 4.15: Phase diagram of r v.s $\dot{r}$ after (a) eleven orbits (b) twelve orbits for $\phi_i = 2\pi/5$.

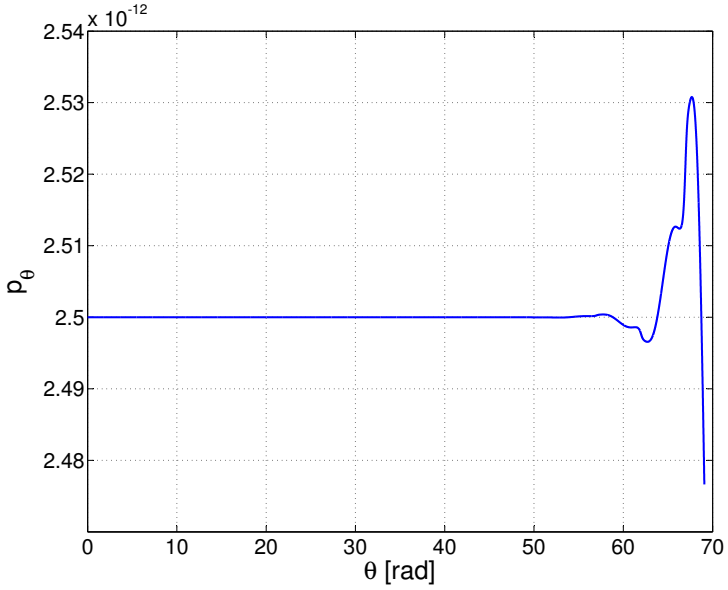

(a)

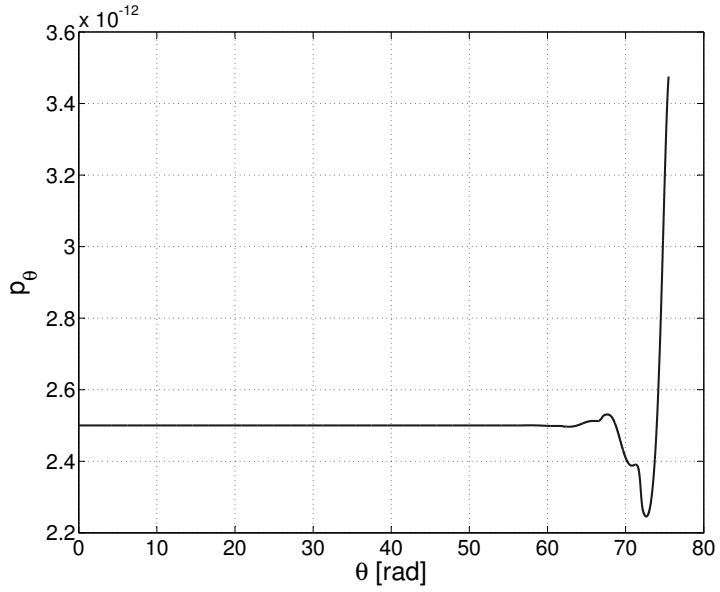

(b)

Figure 4.16: Phase diagram of θ v.s p_θ after (a) eleven orbits (b) twelve orbits for $\phi_i = 2\pi/5$.

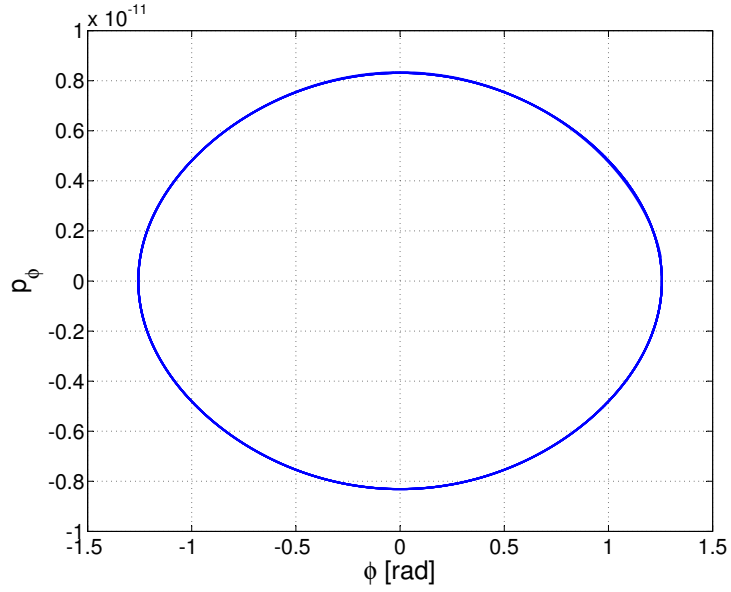

(a)

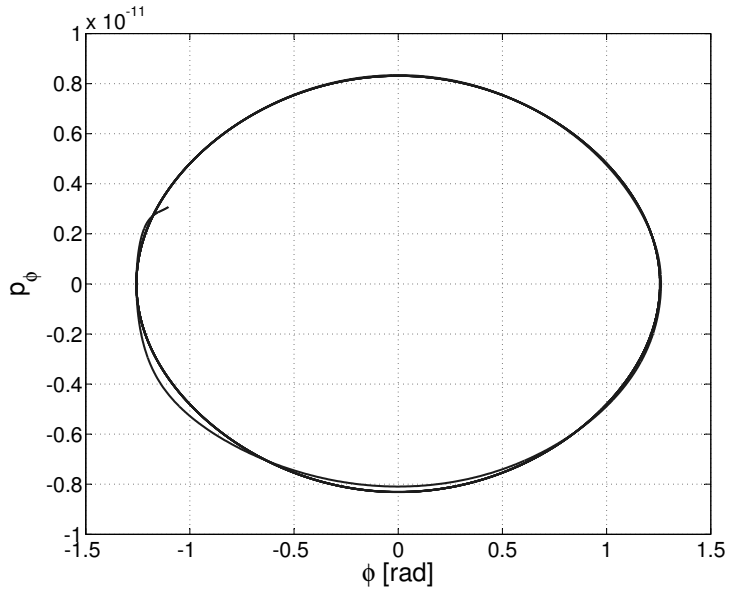

(b)

Figure 4.17: Phase diagram of ϕ v.s p_ϕ after (a) eleven orbits (b) twelve orbits for $\phi_i = 2\pi/5$.

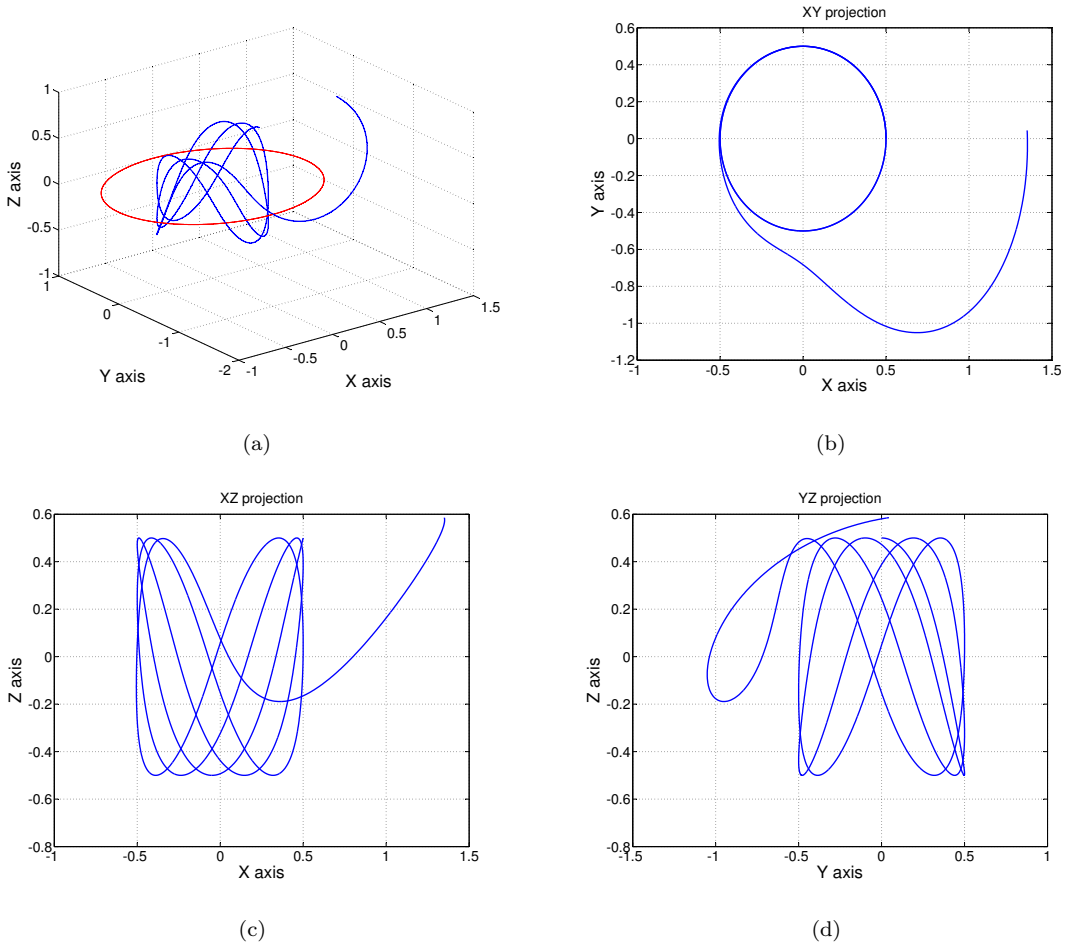

(a) (b)

(c) (d)

Figure 4.18: Simulation of the Sitnikov problem when started from $\phi = \pi/4$ and run for 3 orbits. The red circle in the first figure represents the motion of the second primary body about the first. (a) 3D view (b) X-Y view (c) X-Z view (d) Y-Z view

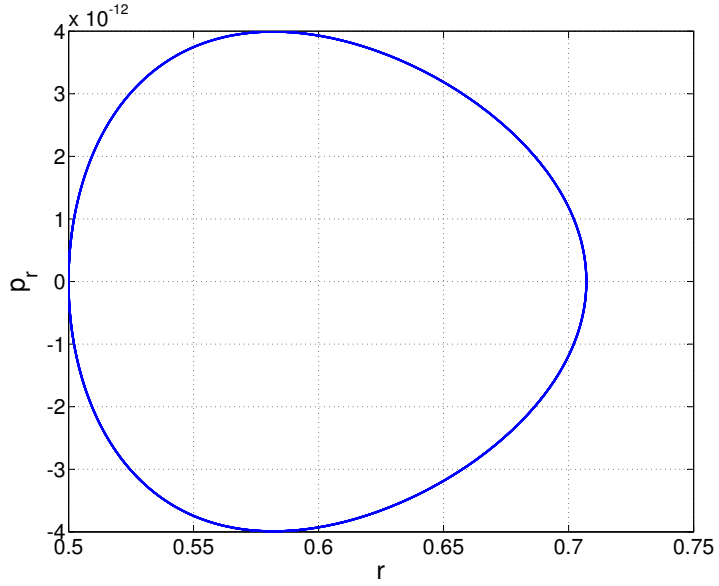

(a)

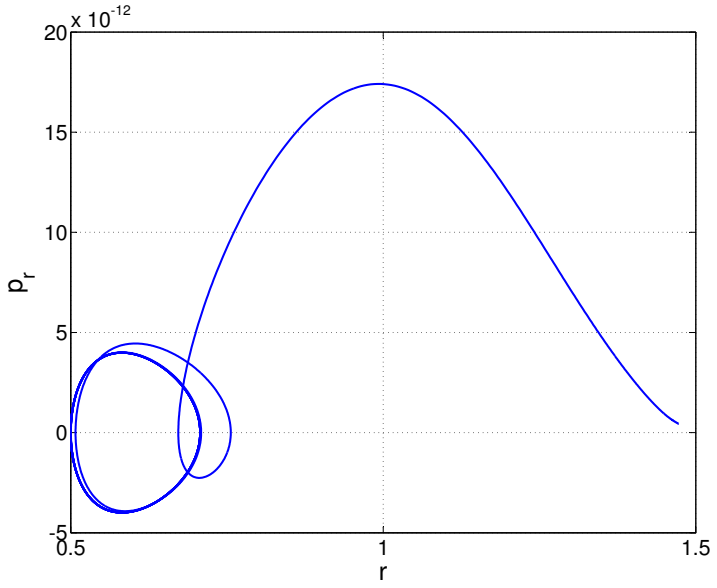

(b)

Figure 4.19: Phase diagram of r v.s $\dot{r}$ after (a) two orbits (b) three orbits for $\phi_i = \pi/4$.

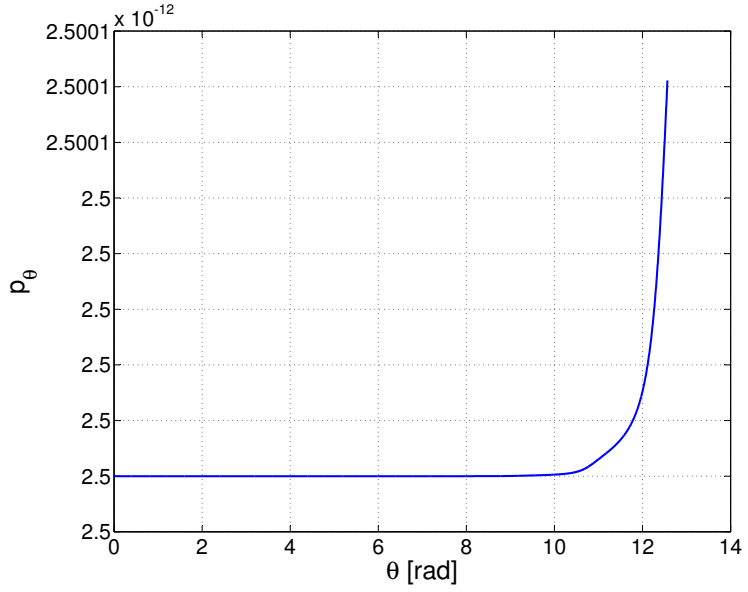

(a)

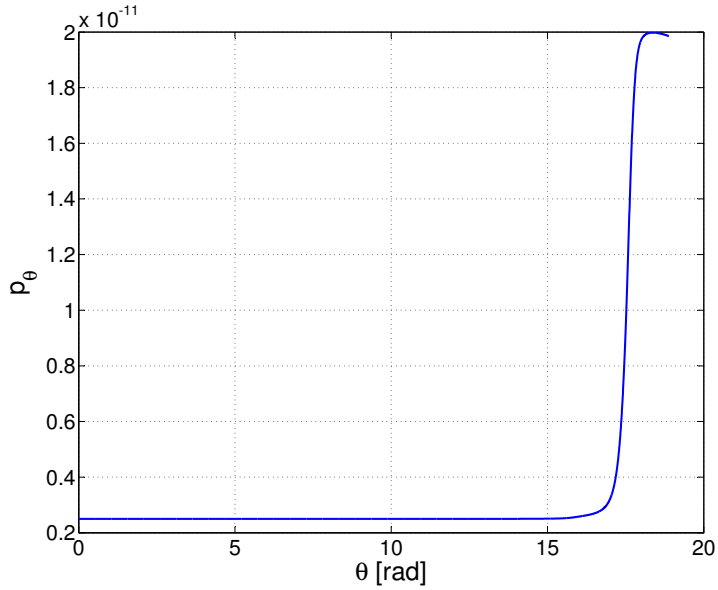

(b)

Figure 4.20: Phase diagram of θ v.s p_θ after (a) two orbits (b) three orbits for $\phi_i = \pi/4$.

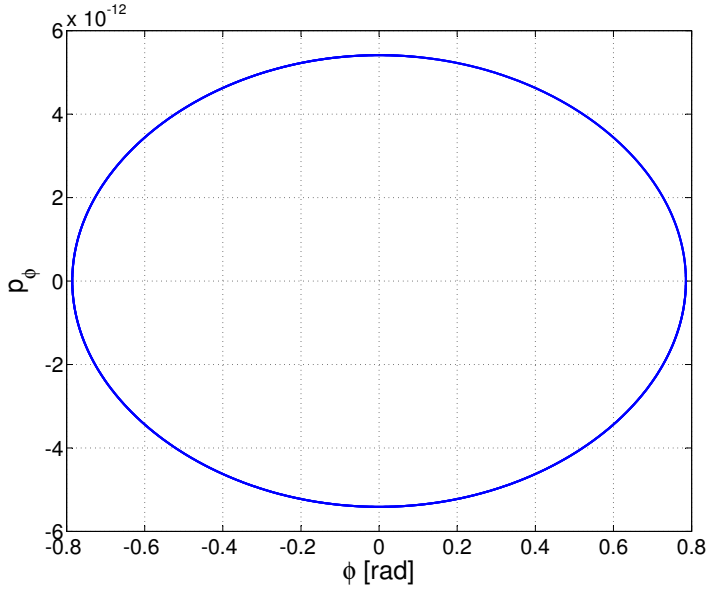

(a)

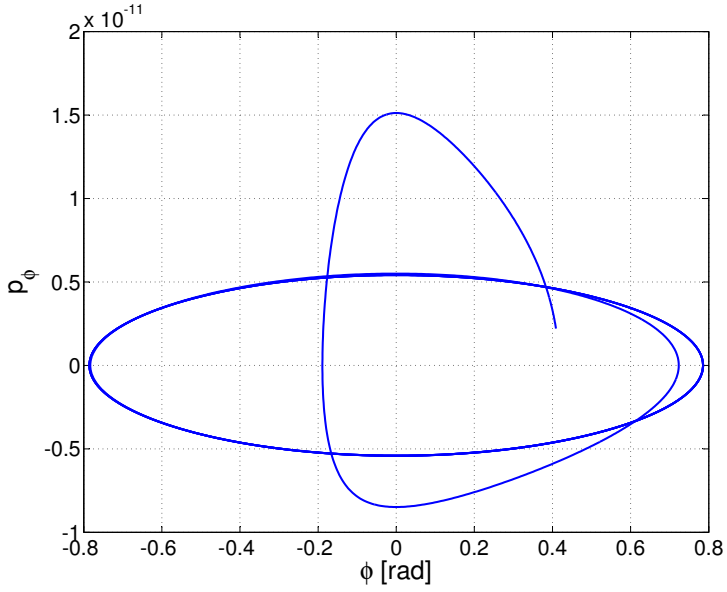

(b)

Figure 4.21: Phase diagram of ϕ v.s p_ϕ after (a) two orbits (b) three orbits for $\phi_i = \pi/4$.

Chapter 5

RESULTS

Now that the model has been set up, Montecarlo simulations are run over the domain of acceptable initial orbital elements in order to gather information about those initial conditions that are the most conducive to increasing the orbital lifetime. A sample simulation is shown in this section. To allow for comparison with the previously presented results (Section 4.2), the perigee height is chosen to be 669.4152 km. Mass is kept constant at 1×10^{-11} kg, while the area used is 32.6087×10^{-17} km^{2*}. This mass is selected since it has the same order of magnitude as the spherical SpaceChip masses in the work of Colombo et. al. [1]. All four perturbations are turned on, ecliptic angle set to 23.4°, and inclination set to 51.6°.

Figure 5.1 shows the change in orbital parameters when eccentricity is varied over $0.01 - 0.8$ and ω over $0° - 360°$. The black shadows at the bottom of the plots indicate the set of initial COE that can be employed to achieve the desired lifespans. For example, if the requirement is to prolong the orbital decay lifetime, energy must be added to orbit, thereby raising its semi-major axis. This can be attained using initial conditions from the shaded area in Figure 5.1(a). It shows that values of argument of perigee between 0 and π radians, coupled with non-circular orbits ($0.1 < e < 0.8$) could help boost the perigee. Acting on this inference, Figure 5.2 was produced to show changes in orbit when ω is kept at a constant low value ($\omega = 0$ rad here), but Ω is varied instead. It shows that selecting the initial eccentricity to be between 0.294 and 0.720, while keeping the longitude of ascending node low ($40° - 72°$) will lead to an increase in semi-major axis.

Similarly, it can be deduced from Figure 5.1(c) that a wide range of eccentricities and argument of perigee can restrict changes in inclination larger than 0.001°, while Figure 5.2(c) indicates that this needs to be paired with values of Ω to be approximately $0,\pi$ or 2π radians at higher eccentricities.

*Corresponds to the characteristics of SpaceChip2 used by Colombo et. al. [1]

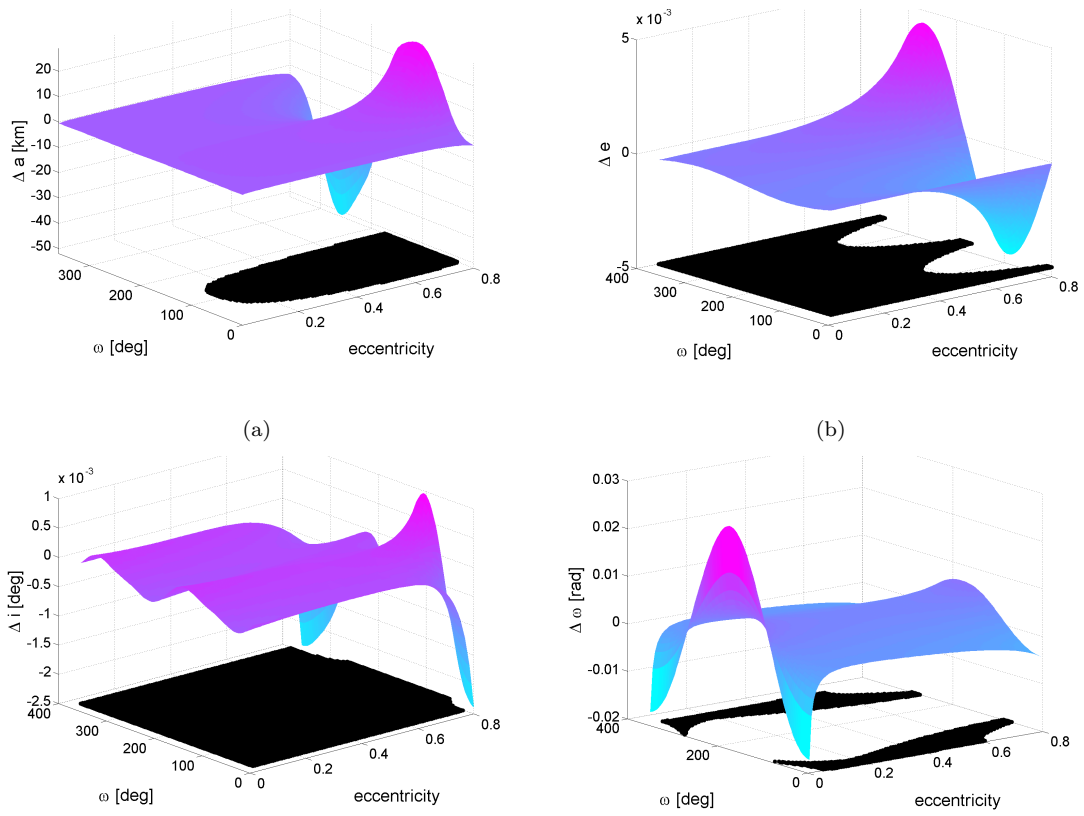

Figure 5.1: Change in orbital parameters over an orbit when started from $h_p = 669.4152$ km, $i = 51.6°$, $\Omega = 0°$, $\lambda = \gamma = 0°$ as eccentricity(e) and argument of perigee (ω) are varied (a) Δ a (km). Black shadow represents the region in $e - \omega$ phase-space that results in $\Delta a > 0$ km. (b) Δ e. Black shadow represents the region in $e - \omega$ phase-space that results in $-0.0001 < \Delta e < 0.0001$. (c) Δ i (deg). Black shadow represents the region in $e - \omega$ phase-space that results in $-0.001° < \Delta i < 0.001°$. (d) $\Delta\omega$ (rad). Black shadow represents the region in $e - \omega$ phase-space that results in -0.001 rad $< \Delta\omega < 0.001$ rad.

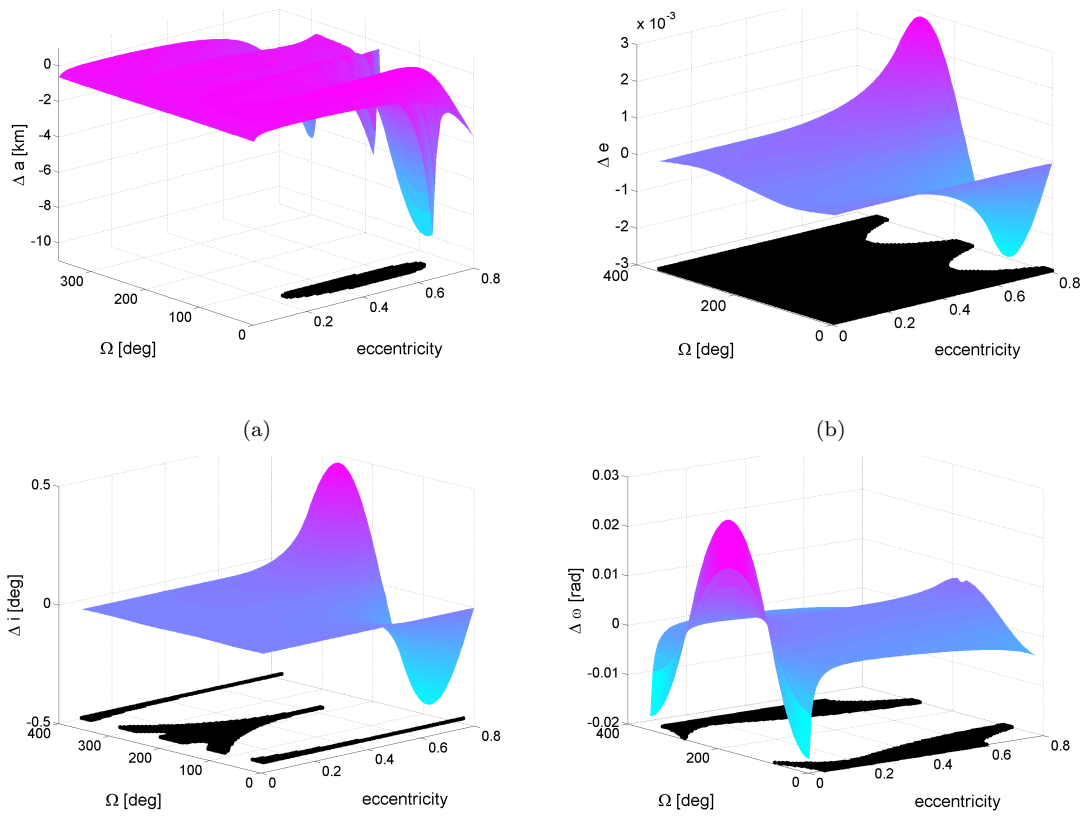

Figure 5.2: Change in orbital parameters over an orbit when started from $h_p = 669.4152$ km, $i = 51.6°$, $\omega = 0°$, $\lambda = \gamma = 0°$ as eccentricity (e) and longitude of ascending node (Ω) are varied (a) Δ a (km). Black shadow represents the region in $e - \Omega$ phase-space that results in $\Delta a > 0$ km. (b) Δ e. Black shadow represents the region in $e - \Omega$ phase-space that results in $-0.0001 < \Delta e < 0.0001$. (c) Δ i (deg). Black shadow represents the region in $e - \Omega$ phase-space that results in $-0.001° < \Delta i < 0.001°$. (d) $\Delta\omega$ (rad). Black shadow represents the region in $e - \Omega$ phase-space that results in -0.001 rad $< \Delta\omega < 0.001$ rad.

In order to demonstrate these conclusions, an arbitrary set of initial conditions is found by superimposing the shadows (referred to henceforth as the 'goldilocks' region) in Figure 5.1 and the lifetime of this orbit determined. It is then compared to another arbitrary set of initial conditions not from the 'goldilocks' region. Table 5.1 shows the parameters of both orbits, while Figures 5.3 - 5.4 show the phase-space evolution of both orbits. The lifetime of the satellite in the orbit selected from this analysis has a lifetime of 338.2627 days, which is over 30 times greater than the other arbitrarily chosen set.

Table 5.1: Comparison of lifetimes from different orbits

	Initial COE	Orbital lifetime
From region of superimposition of the shadows in Figure 5.1	$a = 7047.5752$ km, $i = 51.6°$, $\Omega = 0°$ $e = 0.5287$, $\omega = 25.4545°$ $\lambda = 0°$, $\gamma = 0°$	338.2627 days
From outside the region of superimposition	$a = 7047.5752$ km, $i = 51.6°$, $\Omega = 0°$ $e = 0.0659$, $\omega = 270°$ $\lambda = 0°$, $\gamma = 0°$	10.1771 days

Table 5.1 shows that both, the short and long lifespan orbits, have the same COE with respect to a, i, Ω, λ and γ, and only differ in the values of e and ω. In the case of selecting initial orbital parameters from the 'goldilocks' zone (Figure 5.3), the perigee increases before finally decaying to the height of 250 km, which is the termination condition for the integration. This initial boost of orbit energy is caused by the coupling of the J_2 and solar radiation pressure, while also accounting for the shadow effects and the ecliptic angle. While J_2 can only actuate changes in the values of ω and Ω, these variables are deciding factors of what fraction of each orbit the satellite spends being accelerated by the SRP, rather than being decelerated. In order to increase the altitude of the perigee, the energy gain from SRP must be higher than the orbital energy dissipated by drag. This can be explained by interpreting Figure 5.1(c), which displays that a majority of initial conditions from the $\omega - e$ phase-space yield a positive change in the inclination. Figure 5.4 shows what happens when initial conditions chosen lie outside the goldilocks zone. These graphs appear noisy due to domination of air drag at lower altitudes, which is where most of the life is spent due to the low eccentricity. The trends displayed in them are completely different from those in 5.3, thereby showing that the difference in initial choice of ω and e drastically alters the final orbit decay time.

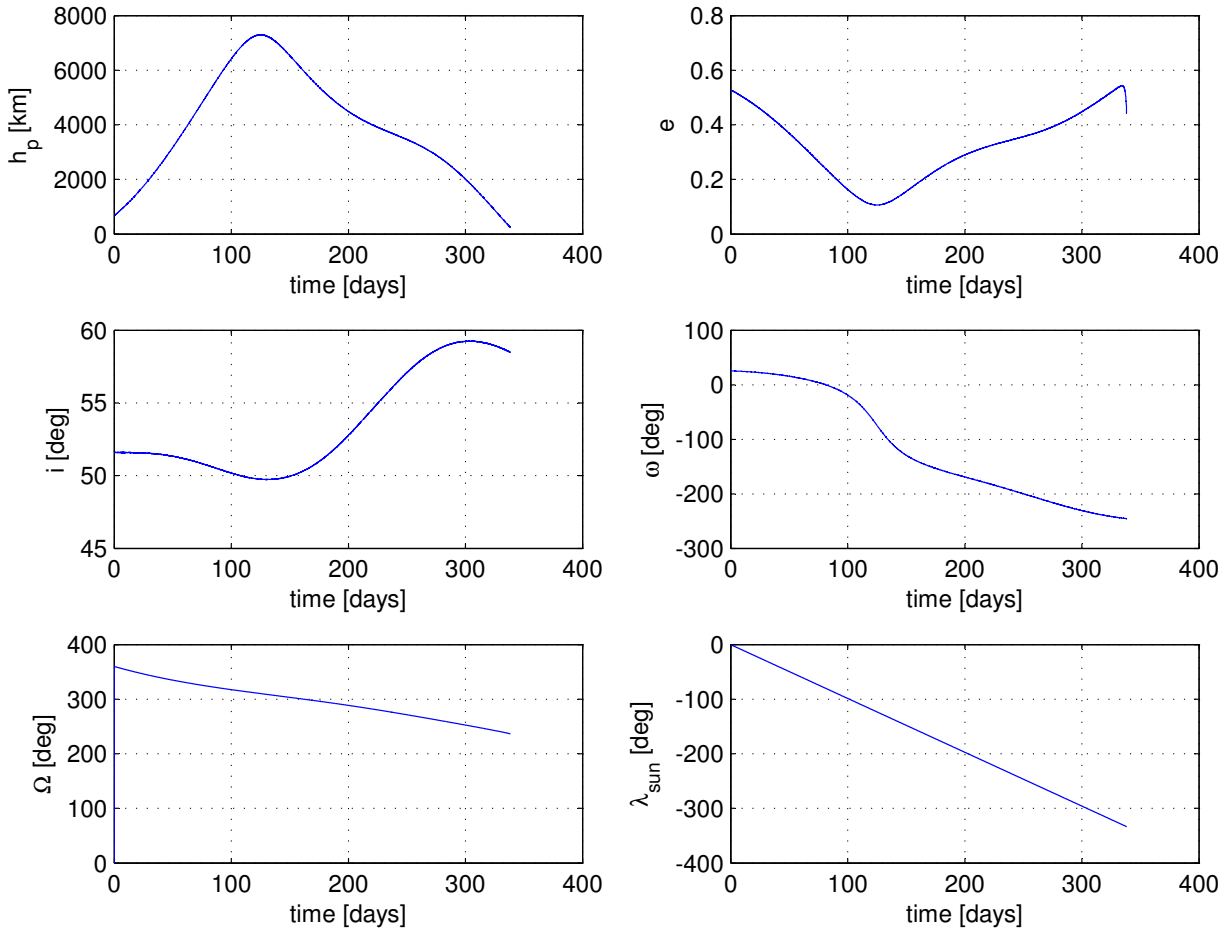

Figure 5.3: Orbit evolution over the entire lifetime when started from those initial conditions that were obtained from superimposing the shadows in Figure 5.1 (i.e. from the 'goldilocks' region).

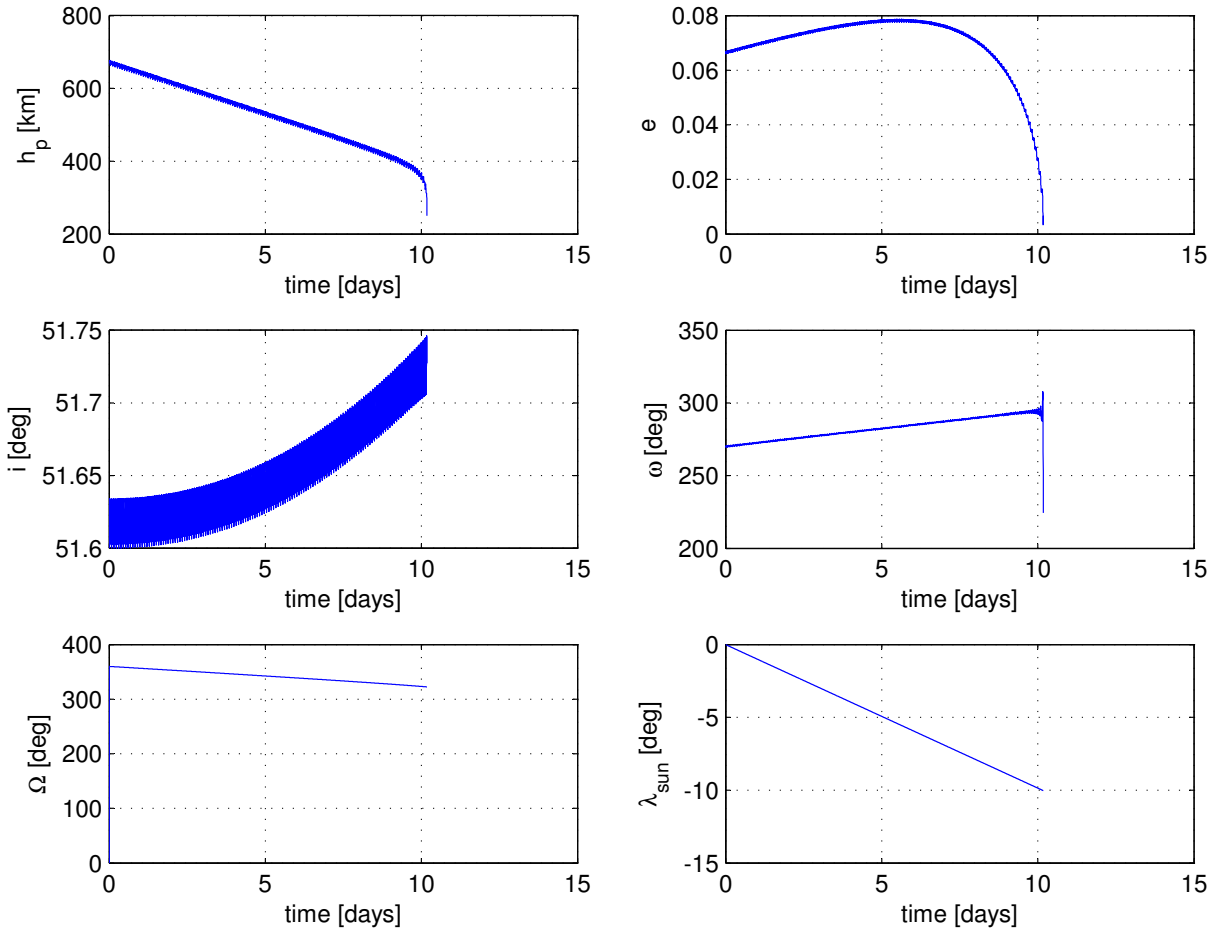

Figure 5.4: Orbit evolution over the entire lifetime when started from initial conditions OUTSIDE the 'goldilocks' region.

Thus, such simulations can be run for a wide range of initial values and the impact of changing initial orbital elements can be assessed to design missions involving satellite swarms with high area-to-mass ratios.

Chapter 6

CONCLUSIONS AND FUTURE WORK

6.1 Conclusions

This document presents a method of selecting desired initial orbital elements that will prolong the orbital lifetime. Montecarlo simulations are able to provide a general intuition for behaviour of orbits in certain regimes. By keeping parameters limited by launch options constant (like a and i) and varying the others over their range of values, the intersection of subsets obtained from each simulation can be shown to be capable of passively balancing various perturbations. The model developed in this thesis calculates the perturbations by atmospheric drag, solar radiation pressure, Earth's J_2 and moon's attraction, while taking into account the Earth's shadow and the obliquity of the ecliptic. All the modelling assumptions and formulations have been validated against existing work.

One of the most prominent inferences from Figures 5.3 - 5.4 is that the dominant perturbing force on satellites of this size is the solar radiation pressure since it has an effect on all the elements of an orbit. Due to the nature of the obliquity of the ecliptic, there is also an increase in inclination, which is further augmented at higher eccentricities. This is logically explained by the existence of an asymmetric projection of the orbital plane to the solar radiation.

Also, the selection of the value of ω plays a prominent role in balancing the drag forces with the SRP forces, given a fixed perigee height and inclination. J_2 is a conservative force and hence it does not cause any secular changes in the semimajor axis. However, J_2 does cause secular changes in ω and Ω, which then induce a change in the fraction of the orbit time spent being accelerated by SRP, rather than decelerated. The spherically-symmetric nature of the atmospheric model embedded in this model allows for only dissipative changes in a, which is balanced by the energy addition from SRP in some cases. Drag aims to circularize the orbit, while SRP can impose periodic changes in eccentricity.

This body of work analyses the possibility of selecting initial orbits for particle-sized satellites (high area-to-mass ratio) such that the effects due to SRP, drag, J_2 and Moon's perturbations will balance out to result in desired lifespans without active control. The direct use of Hamiltonian equations enables the

addition of perturbing forces other than those included in this study. A number of moons may be added, while their ecliptic orbits and/or inclinations around the central body may also be defined appropriately by making changes to the equations of motion. The method and formulations used here can also be applied to different systems, for example, lunar satellites. The ecliptic angle can also be changed to use this model for other planetary bodies.

6.2 Recommendations for future work

Two prospective paths can be considered in the progress of this project – improvisation of the model itself, and the fields of application of this model. Improving the model is often based on refining the assumptions; the following are some of the recommendations for doing so:

- *Jacchia-Roberts atmospheric model*

  The exponential model for approximating the atmospheric density is terribly inaccurate for heights above 200 km. The Jacchia-Roberts model, coupled with diffusion equation, gives the density of air as a function of position, time, solar activity and geomagnetic activity [3]. There exist other models of varying accuracy, and can be coded in depending on the kind of simulated mission.

- *Deeper analysis of eclipses by central body*

  Ignoring of the parallax can be enough for simulation of Low-Earth orbits; however, a more comprehensive model could look at conical shadows, and correspondingly at the effect of penumbras. A step further would be the ability to include the eclipsing due to the planetary moon.

- *Variational integrators*

  Variational integrators respect the geometric properties of the system being analysed. These integrators discretize the variational formulation and have been shown to be equal or better than traditional integrators in many cases [15][16].

- *Other perturbing forces*

  If this model is extended to planetary rings, forces like electromagnetic attractions, albedo and infrared radiation, and Sun's attraction will also be needed to be considered for precise simulations.

- *Removal of singularities*

  To overcome the disadvantage of the possibility of singularities due to the use of spherical coordinate system (refer Chapter 1 and Eq. 2.2), a master governor code can be written to switch the entire formulation to use the colatitude in Eq. 2.2 as ϕ, and not the complement of the colatitude.

Another avenue for future work can be to vary the application of the work developed here. Some of them can be as follows:

- *Effects of changing initial altitude/semi-major axis*

  All the results in Chapter 5 correspond to the initial perigee altitude of 669.4152 km. However, the perigee altitude may be an influential factor in changing the trends of orbit evolution. The behaviour of other elements will tend to change with an increase/decrease in perigee height due to change in the drag.

- *Planetary ring formations*

  The application of this thesis to the study of formation and orbit evolution of the planetary rings is the desired goal. Higher computational resources would have to be allocated to proceed with this work, while also improving upon the assumptions and adding perturbations like electromagnetic forces into the model.

- *Dust particle orbits about Sun-Jupiter L_4 and L_5 points*

  Without external perturbations, the particles in orbit at the L_4 and L_5 Lagrange points follow stable trajectories in the circularly-restricted framework. Potential effort could be directed at simulating orbits at these points while under the combined influence of other forces.

References

[1] C. Colombo and C. McInnes, "Orbital dynamics of "smart-dust" devices with solar radiation pressure and drag," *Journal of Guidance, Control, and Dynamics*, vol. 34, no. 6, pp. 1613–1631, 2011.

[2] M. T. Lane, "On analytic modeling of lunar perturbations of artificial satellites of the earth," *Celestial Mechanics and Dynamical Astronomy*, vol. 46, no. 4, pp. 287–305, 1989.

[3] D. A. Vallado, *Fundamentals of Astrodynamics and Applications*. Microcosm Press and Springer, 2007.

[4] L. J. Giovanni Vulpetti and G. L. Matloff, *Solar Sails: A Novel Approach to Interplanetary Travel*. Springer, July 2008.

[5] P. Musen, R. Bryant, and A. Bailie, "Perturbations in perigee height of vanguard i," *Science*, vol. 131, no. 3404, pp. 935–936, 1960.

[6] M. Horanyi, J. A. Burns, and D. P. Hamilton, "The dynamics of saturn's e ring particles," *Icarus*, vol. 97, no. 2, pp. 248 – 259, 1992.

[7] T. Vladimirova, X. Wu, K. Sidibeh, D. Barnhart, and A. . Jallad, "Enabling technologies for distributed picosatellite missions in leo," in *Proceedings - First NASA/ESA Conference on Adaptive Hardware and Systems, AHS 2006*, vol. 2006, 2006, pp. 330–337.

[8] B. A. Warneke and K. S. J. Pister, "Mems for distributed wireless sensor networks," in *Proceedings of the IEEE International Conference on Electronics, Circuits, and Systems*, vol. 1, 2002, pp. 291–294.

[9] C. Colombo and C. McInnes, "Orbit design for future spacechip swarm missions in a planetary atmosphere," *Acta Astronautica*, vol. 75, pp. 25–41, 2012.

[10] J. E. Prussing and B. A. Conway, *Orbital Mechanics*. Oxford-University Press, 1993.

[11] L. Blitzer, *Handbook of Orbital Perturbations*. University of Arizona, 1970.

[12] J. O'Keefe, A. Eckels, and R. Squires, "The gravitational field of the earth," *The Astronomical Journal*, p. 245, 1959.

[13] K. Sitnikov, "The existence of oscillatory motions in the three-body problem," *Doklady Akademii Nauk SSSR*, vol. 133, no. 2, pp. 303–306, 1960.

[14] M. Gidea and F. Deppe, "Chaotic orbits in a restricted three-body problem: Numerical experiments and heuristics," *Communications in Nonlinear Science and Numerical Simulation*, vol. 11, no. 2, pp. 161–171, 2006.

[15] M. West, "Variational integrators," Ph.D. dissertation, California Institute of Technology, 2003.

[16] C. Kane, J. E. Marsden, M. Ortiz, and M. West, "Variational integrators and the newmark algorithm for conservative and dissipative mechanical systems," *International Journal for Numerical Methods in Engineering*, vol. 49, no. 10, pp. 1295–1325, 2000.